

A modular quantum computer based on a quantum state router

Chao Zhou^{1†}, Pinlei Lu^{1†}, Matthieu Praquin², Tzu-Chiao Chien¹, Ryan Kaufman¹, Xi Cao¹, Mingkang Xia¹, Roger S. K. Mong¹, Wolfgang Pfaff³, David Pekker¹, Michael Hatridge¹

¹Department of Physics and Astronomy, University of Pittsburgh, Pittsburgh, PA, USA

²Département de Physique, École Normale Supérieure, Paris, France

³Department of Physics, University of Illinois at Urbana-Champaign, Urbana, IL, USA

†These authors contributed equally to this publication.

(Dated: November 17, 2022)

A central challenge for realizing large-scale quantum processors is the design and realization of qubit-qubit connectivity. On the one hand, these connections need to be strong enough to enable fast two-qubit gates, while on the other hand, they must be well-confined between modes to avoid extra loss and cross-talk errors. Finally, we also desire the connections to be made in a "detachable" way, so that different parts of the processor can be built/tested/replaced individually. In this work, we present a microwave quantum state router that realizes all-to-all couplings among four independent and detachable quantum modules of superconducting qubits. Each module consists of a single transmon, readout mode, and communication mode coupled to the router. The router design centers on a parametrically driven, Josephson-junction based three-wave mixing element which generates photon exchange among the modules' communication modes. We first demonstrate coherent photon exchange among four communication modes, with an average full-*i*SWAP time of 760 ns and average inter-module gate fidelity of 0.97, limited by our modes' coherence times. We also demonstrate photon transfer and pairwise entanglement between the modules' qubits, and parallel operation of simultaneous *i*SWAPs across the router. The gates demonstrated here can readily be extended to faster and higher-fidelity router operations, as well as scaled to support larger networks of quantum modules.

I. INTRODUCTION

Building quantum information processors of increasing size and complexity requires meticulous management of both the qubits' environment and qubit-qubit interactions. Suppressing interaction with the external environment has always been recognized as the central difficulty in maintaining coherence in a system. In the long term, this challenge will be met by fault tolerantly encoding much smaller logical machines inside a qubit fabric. In the present so-called Noisy Intermediate-Scale Quantum (NISQ) era, we must simply run short circuits. However, in both the short and long term, we face choices about which architecture of machine we build. In large-scale processors based on a monolithic fabric of nearest-neighbor interactions, the circuit topology/connectivity must be carefully designed to avoid spectator qubit errors and long-range cross-talk^{1–3}. In addition, we face the challenge of fabricating all components to perform flawlessly on a single die⁴.

Modular quantum systems offer a very promising alternate route to large-scale quantum computers, allowing us to sidestep many of these difficulties and instead operate using smaller, simpler quantum modules linked via quantum communication channels^{5–8}. Such machines allow us to replace faulty components and test sub-units separately, which can greatly ease requirements for flawless fabrication while also allowing distant qubits to communicate with many fewer intermediate steps, potentially enhancing fidelity in near-term quantum processors⁹. Moreover, the quasi-particles that cause additional bit flip and phase flip errors would also be constrained inside the module instead of propagating across the whole

monolithic processor, reducing correlated errors in modular structures^{10,11}.

The key element that determines the performance of a modular machine is its quantum communication bus. For atomic scale qubits (which form the basis for many of the early proposals for modular quantum computing) communicating using optical-frequency states, it is infeasible to couple photons into a communication channel with very high efficiency. This loss of information precludes light from simply being transferred from module to module. Instead, one must herald instances in which transmission is successful^{12–16}. However, once light has been coupled into an optical fiber, it can be readily distributed over kilometer and longer distances, which readily supports long-range entangled state generation and distributed quantum computation^{17,18}. In superconducting circuits, there have also been several recent demonstrations of similar measurement-based protocols^{19–22}.

However, superconducting circuits can also transfer states directly. For this form of direct state exchange, we require strong, switchable couplings from module to the communication channel to enable rapid operations, low losses in the channel, and a dense, reconfigurable network of couplings among many modules^{23,24}. Realizations to date have focused on pairs of quantum modules^{25–29} or modes in a monolithic device^{30–34}. They have utilized transmission-line based 'quantum bus' communication channels and controllable module-bus couplings based on the nonlinearity of Josephson junctions or driven exchange via a driven, nonlinear coupling mode.

In this article, we propose and experimentally implement a new scheme for creating a modular superconducting network, which instead creates a nonlinear 'quantum

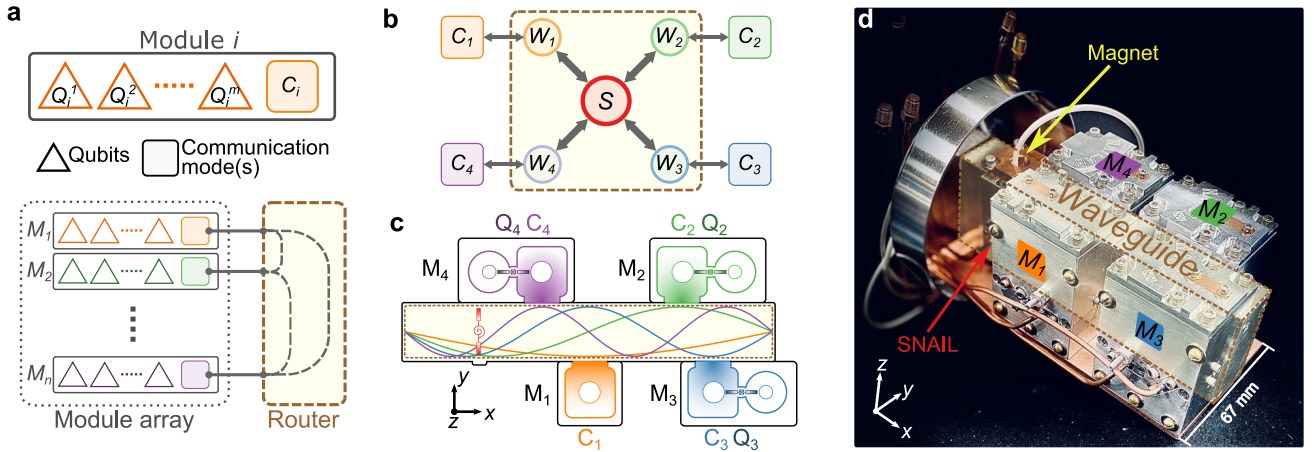


Figure 1. Schematic representation and picture of the modular quantum computer device. (a) Basic structure of our modular quantum computer, in which a number of quantum modules are connected via their communication modes to a quantum state router. (b) Coupling scheme between the router and four communication modes. The brown dashed square represents the router with four waveguide modes (W_1 – W_4) and a SNAIL (S). Each waveguide mode is dispersively coupled to a single communication cavity mode (C_1 – C_4). (c) Schematic drawing of the full system consisting of four modules and the central quantum state router. The colored curves inside the router represent the electric field (E) of the first four waveguide TE_{10n} ($n = 1, 2, 3, 4$) eigenmodes. Since each waveguide mode has a different E -field distribution and the SNAIL mode is detuned differently from each waveguide mode, we can place the SNAIL chip (represented in red) at a location where it has different coupling strengths $g_{w,s}$, but similar hybridization strengths $(\frac{g}{\Delta})_{w,s}$, to each waveguide mode. Each module (for M_2 to M_4) consists of a qubit (Q_2 – Q_4), a communication cavity (C_2 – C_4) and a readout cavity (in module M_1 the qubit has been omitted). Each communication cavity is designed to have a frequency that is close to one waveguide mode and far away from the others to ensure a desired hybridization strength to the router. (d) Photograph of the assembled device.

state router' with fixed, dispersive couplings to individual quantum modules. The strong, parametrically driven nonlinearity of the quantum state router allows us to only virtually occupy its modes, and thus achieve efficient operations over the router with only modest requirements for router quality. There is no use of measurement in the router system; operations over the bus can be thought of as direct, parametrically actuated gates between quantum modules. The state router naturally supports all-to-all coupling among several quantum modules, and is naturally extensible to a larger modular network. We have realized the quantum state router using a Superconducting Nonlinear Asymmetric Inductive eElement (SNAIL)-based nonlinearity³⁵, and used it to operate a four module quantum processor.

II. THEORY OF ROUTER OPERATION

The basic structure of our modular quantum computer consists of two major parts: a quantum state router and multiple modules, as shown in Figure 1. Each module consists of a variable number of qubits (one in our present experiment) which have controllable, local coupling with each other. In each module, there should also be at least one ‘communication’ mode which couples to both the qubits in the module and the quantum state router. This communication mode can either be a qubit or, as in this work, a long-lived harmonic oscillator which

can store information for exchange over the router.

We have realized our modular quantum computer as a 3D superconducting circuit, and have adopted several design rules to guide our efforts. First, the communication modes we use are superconducting 3D cavities rather than qubits, as they accommodate multiple qubit encoding schemes including the Fock encoding used in this work, cat states³⁶, binomial encodings³⁷, GKP-encodings³⁸, etc. This allows our router to be compatible with a wide array of future module designs. Second, we emphasize the “modularity” of our system in the additional sense that each module and the router itself exist as independent units which can operate individually, instead of the whole system forming a monolithic block. This offers a tremendous advantage in the laboratory, as defective components can be easily replaced, and the different components can be tested separately and then assembled. Third, the router operates via coherent photon exchange based on parametric driving of a 3-wave-mixing Hamiltonian, in which the third-order nonlinearity is introduced by a SNAIL device. Finally, we have designed the router to minimize both the need for precise frequency matching between router and module modes, and minimize the requirements for high-Q router elements. To accomplish this, we couple all modes in the system dispersively.

The only nonlinear element is a central SNAIL-mode S (with corresponding annihilation operator \hat{s}), which is very strongly coupled to an input line for strong paramet-

ric driving, and flux biased via a nearby copper-sheathed electromagnet. As such, it has a low quality factor Q ($\sim 10,000$). The remainder of the router is composed of a rectangular, superconducting 3D waveguide. The first four transverse electric modes ($TE_{10i}, i = 1, 2, 3, 4$) of the waveguide W_i (with annihilation operators \hat{w}_i) are each used as an intermediate mode coupling to both the SAIL and a corresponding communication mode C_i (with operator \hat{c}_i in the i^{th} module). The SAIL is flux biased to a point where its even-order nonlinear terms are negligible^{35,39} and the third-order term is strong, resulting in the Hamiltonian of the router, which is separated into mode energies, interactions, and nonlinear terms, respectively:

$$\begin{aligned}\hat{\mathcal{H}}_R/\hbar &= \hat{\mathcal{H}}_{R,0}/\hbar + \hat{\mathcal{H}}_{R,\text{int}}/\hbar + \hat{\mathcal{H}}_{R,\text{nl}}/\hbar \quad (1) \\ &= \left[\omega_s \hat{s}^\dagger \hat{s} + \sum_i \omega_{w_i} \hat{w}_i^\dagger \hat{w}_i \right] + \left[\sum_i g_{w_i s} (\hat{w}_i^\dagger \hat{s} + \hat{w}_i \hat{s}^\dagger) \right] \\ &\quad + [g_{sss} (\hat{s} + \hat{s}^\dagger)^3].\end{aligned}$$

The waveguide modes are naturally orthogonal; each is coupled to the SAIL with strength $g_{w_i s}$, and g_{sss} is the strength of the SAIL's third-order term. We parametrically drive photon exchange between a pair of waveguide modes by driving the SAIL at the difference of their frequencies. This scheme has been long used in parametric amplifiers and circulators, where it goes by the name 'noiseless photon conversion'⁴⁰⁻⁴². To have independently controllable couplings, we have chosen the SAIL frequency and waveguide dimensions so that all mode frequencies and frequency differences are unique, with all difference frequencies below the lowest mode frequency (see Supplementary Information section I, Fig. S1).

As all frequencies are widely separated, we can rediagonalize the system to eliminate the interaction term, slightly shifting all mode frequencies and definitions (for simplicity's sake, we omit any change of variable representation for the new, hybrid eigenmodes), and inducing all possible self- and cross-three-wave couplings among the waveguide modes and SAIL. This is analogous to common techniques used in circuit QED^{43,44}, with a third- rather than fourth-order nonlinearity. Retaining only the parametric coupling terms we will use in the router, which is safe as long as all other processes are well separated from any desired process in frequency, we write the effective Hamiltonian of the router as

$$\hat{\mathcal{H}}_R^{\text{eff}}/\hbar = \hat{\mathcal{H}}_{R,0}/\hbar + \sum_{i \neq j} g_{w_i w_j s}^{\text{eff}} (\hat{w}_i^\dagger \hat{w}_j \hat{s} + \hat{w}_i \hat{w}_j^\dagger \hat{s}^\dagger). \quad (2)$$

The effective three-wave interaction strengths are given by $g_{w_i w_j s}^{\text{eff}} \approx 6g_{sss}(\frac{g}{\Delta})_{w_i s}(\frac{g}{\Delta})_{w_j s}$, where $\Delta_{w_i s} = \omega_{w_i} - \omega_s$. We note that in our experiment, we never directly populate these waveguide modes or drive their difference frequencies. Instead, these terms serve as a 'scaffold' in the

router to create similar terms among the module communication modes, as detailed below. The hybridization strengths $(\frac{g}{\Delta})_{w_i s}$ are key parameters, as they both limit the eventual parametric coupling strengths and determine how much longer-lived the waveguide modes can be compared to the low- Q SAIL mode.

Next, we combine our router with the modules' communication modes. As shown in Fig. 1b, we accomplish this by creating four modules, each containing one mode with a frequency near one of the router's waveguide modes, and coupling to the router via an aperture in their shared wall. This coupling is deliberately dispersive, with the strength controlled by a combination of waveguide-communication mode detuning, coupling aperture size, and placement along the router's length. Assuming each cavity is only coupled to its "adjacent" waveguide mode, the router plus communication mode Hamiltonian is written as:

$$\begin{aligned}\hat{\mathcal{H}}_{RC}/\hbar &= \hat{\mathcal{H}}_R/\hbar + \hat{\mathcal{H}}_{C,0}/\hbar + \hat{\mathcal{H}}_{RC,\text{int}}/\hbar \quad (3) \\ &= \hat{\mathcal{H}}_R/\hbar + \left[\sum_i \omega_{c_i} \hat{c}_i^\dagger \hat{c}_i \right] + \left[\sum_i g_{c_i w_i} (\hat{c}_i^\dagger \hat{w}_i + \hat{c}_i \hat{w}_i^\dagger) \right].\end{aligned}$$

The second and third terms denote the communication mode's energy and the communication mode-waveguide mode interactions, respectively. As before, we diagonalize this Hamiltonian to eliminate the direct interactions among the modes without changing variable representation, and neglect all but the cavity-cavity third-order interactions to find the new effective Hamiltonian for the composite router plus communication modes system:

$$\hat{\mathcal{H}}_{RC}^{\text{eff}}/\hbar = \hat{\mathcal{H}}_{R,0}/\hbar + \hat{\mathcal{H}}_{C,0}/\hbar + \sum_{i \neq j} g_{c_i c_j s}^{\text{eff}} (\hat{c}_i^\dagger \hat{c}_j \hat{s} + \hat{c}_i \hat{c}_j^\dagger \hat{s}^\dagger). \quad (4)$$

The resulting effective three-body interaction strength is $g_{c_i c_j s}^{\text{eff}} \approx g_{w_i w_j s}^{\text{eff}} (\frac{g}{\Delta})_{c_i w_i} (\frac{g}{\Delta})_{c_j w_j}$.

The use of a network of hybridization, linking the cavity modes to the central SAIL via intermediate cavity modes comes with advantages: Since the SAIL pump port is physically separated from the communication modes in two different metal bodies, we can assume no direct coupling between them. Thus, by choosing each dispersive coupling $g/\Delta \simeq 0.1$, the weakly hybridized communication modes can live up to 10^4 times longer than the SAIL mode and 100 times longer than the waveguide modes, greatly decreasing the need for long lifetime components in the router.

Moreover, dispersive couplings and parametric driving are insensitive to modest errors in mode frequencies, further reducing the need for precision fabrication, unlike photon exchange techniques based on resonant mode couplings^{28,45}. While it is certainly possible to remove the intermediate waveguide modes in a monolithic version of our design, this comes with both greatly reduced flexibility in combining disparate elements and more stringent requirements for the SAIL's lifetime.

In operation, the parametrically driven two-body exchange rate, for example between modes C_i and C_j , is $\sqrt{n_s}g_{c_i c_j s}^{\text{eff}}$, where n_s is the pump strength expressed as a photon number (see SI Sec. III.A). It is here that we find the price for our hybridization network: the effective three body coupling has been greatly reduced ($g_{c_i c_j s}^{\text{eff}} \simeq 6 \times 10^{-4} g_{sss}$). To achieve rapid gates with feasible pump strengths, we must both engineer g_{sss} to be large and carefully design the pump line (and the SAIL itself) to tolerate very strong drives to compensate for this dilution of nonlinearity.

It is also important to note that Eq. 4 represents only our desired coupling terms. In practice, all modes inherit both self- and cross-three-wave mixing terms from the SAIL. Of particular concern are couplings between a cavity and non-adjacent waveguide modes (e.g. C_3 to W_4). To avoid potential issues, we choose a minimum waveguide to cavity spacing of ~ 100 MHz to suppress cross-talk with these couplings. This difference frequency is comparable to the anharmonicity of transmon qubits; similarly, we can use variants of the DRAG⁴⁶ technique to drive rapid *i*SWAP gates among the communication modes without leakage to unwanted modes (see SI Sec. VI).

III. RESULTS

Basic router characterization with coherent states. For initial experiments, we connect our router to four simple modules (see SI Sec. I and Methods for details), but omit the module qubits. Each communication mode is driven and read out via a ‘weak’ port whose induced relaxation rate is much smaller than the mode’s internal loss rate. Figure 2a shows an experimental pulse sequence for swapping coherent states between the module communication modes C_2 and C_4 . First, a short on-resonance drive is applied to C_4 through the weakly coupled port, which creates a coherent state in this cavity. Then, a pump tone is applied to the SAIL mode near the $C_2 - C_4$ difference frequency $\omega_p = \omega_{c_4} - \omega_{c_2} + \delta$, where δ is the pump detuning relative to the measured frequency difference between the two cavity modes. Meanwhile, the light in these two cavities is monitored by receiving the I-Q voltage leaking out from each cavity’s weakly coupled port. By varying the applied pump frequency and time, we can determine both the swap rate and resonant condition for pumping.

The experiment results are shown in Fig. 2b, c. There is good agreement between the envelope of the swap trace (green and purple lines) and the hybridized decay trace, indicating that the state is only swapping between these two cavities without leaking into other modes, and that the fidelity of state exchange is mainly limited by the lifetime of these two cavities. This same experiment is then performed for the six possible pairs of the four communication modes. We find the fastest full-swap time to be 375 ns, the slowest 1248 ns, and an average swap time of

~ 760 ns (see SI Sec. III.B). For each pair, the maximum gate speed is measured by increasing the pumping power until we see the mode coherence times substantially differ from their undriven values. On average, the pump frequency required to fully swap light between the two cavities is detuned by several hundred kHz (-416 kHz for the data in Figure 2). We attribute this to a combination of SAIL- and communication-mode static and dynamic Kerr effects; that is, the communication-mode frequencies are shifted due to the off-resonance pump on the SAIL mode. In our pulses, we are only sensitive to changes in the communication modes’ frequency difference, so shifts can be positive/negative/zero depending on whether the two modes shift closer together or further apart. This has strong parallels to saturation effects in parametric amplifiers^{39,47-49}, though here the primary consequence is simply that we must track these shifts in our control electronics.

Operation as a modular quantum computer with single-qubit modules. Next, we add the transmon qubits to complete modules 2-4 (module 1’s qubit is omitted), and operate the full device as a small, modular, quantum computer. Each single-qubit module consists of one communication cavity C_i , one transmon Q_i , and one readout cavity R_i . The machine’s layout is shown schematically in Fig. 1c. For simplicity, our qubit states throughout the system are the Fock states $|0\rangle$ and $|1\rangle$, although the communication modes could in principle support a variety of more complex encodings. We perform intra-module gates between the qubit and cavity in each module using a doubly-driven parametric photon exchange process (see^{20,25,50} and SI Sec. IV for details), which are indicated as paired drives in Fig. 3b.

In the simple algorithms that follow, we refer to the operation of these exchange interactions as variations of the *i*SWAP gate, as is typical for gates based on coherent photon exchange^{20,30,31,34,50,51}. We exclusively use these gates to swap coherent states or Fock states fully from a source cavity to a formerly empty target cavity. In this scenario, the gates act as a combination of SWAP and z -rotation for both Fock and coherent states. However, this analogy breaks down for both intra- and inter-module exchange of Fock states between a qubit and cavity and a pair of cavities, when we consider arbitrary pulse lengths and certain joint qubit-cavity or cavity-cavity Fock states (e.g. $|1, 1\rangle$). For this reason, some researchers choose to refer to such gates between pairs of cavities as ‘beam splitters’^{50,52} for their obvious resemblance to the optical component of the same name. This analogy, however, fails for our qubit-cavity interactions, so we choose instead to refer to these gates via the exponent which determines their unitary relative to a full *i*SWAP gate, i.e., a $\sqrt{i\text{SWAP}}$ is described by $U_{i\text{SWAP}}^{\frac{1}{2}}$. Because our protocols only swap light into empty qubits/cavities, states containing two or more photons are never occupied. As such, this inexact analogy yields both a simple graphical and conceptual picture of our gates, as well as correct intuition about the system’s evolution during our proto-

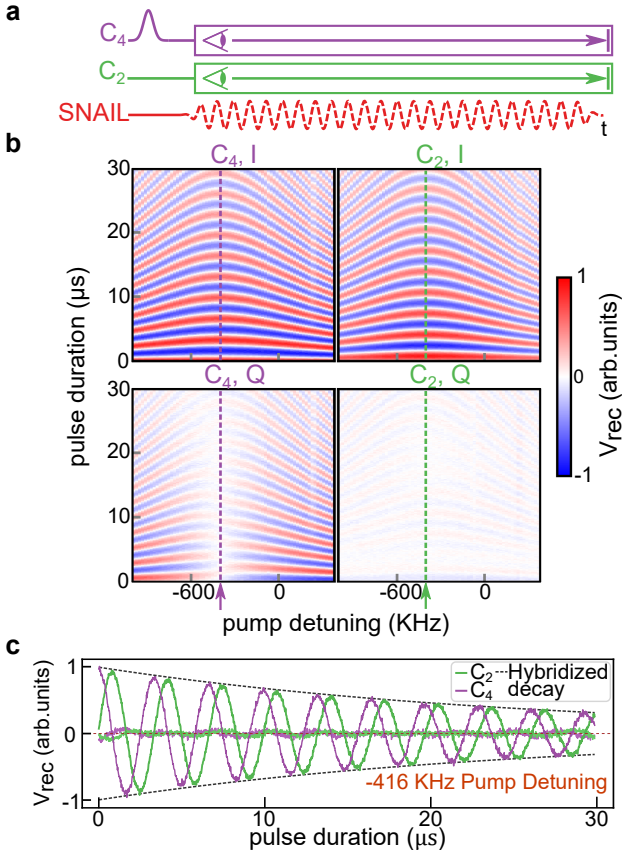


Figure 2. Coherent state exchange between communication cavities. (a) Pulse sequence of the swap experiment. We begin by displacing one cavity to create a coherent state, which we then swap between a pair of cavities by applying a parametric drive to the SQUID. We continuously monitor the I-Q voltage in each cavity during the swap process. (b) In-phase and quadrature received voltage from the two cavities versus pulse duration and pump detuning from the nominal difference frequency. The dashed vertical line denotes the optimal detuning frequency for full photon exchange. (c) Line-cut of (b) at the optimal full-swap detuning. The grey dashed envelope represents the theoretical hybridized T_2 decoherence trace of C_2 and C_4 , given by $\exp[-t(\Gamma_2 + \Gamma_4)/2]$, where Γ_2 and Γ_4 are the decoherence rates of C_2 and C_4 , respectively.

cols. This issue, however, must obviously be revisited for alternate qubit encoding choices, and when both send- and receive-modes are in arbitrary states. For further discussion see SI Sec. II.

We next use the module transmons and intra-module $i\text{SWAP}$ operations to swap Fock states across the router, transferring single photons between distant qubits as shown in Fig. 3a, b. The protocol begins with all qubits and cavities prepared in their ground states. A $R_x(\pi)$ pulse is first applied to Q_2 which brings it to the excited state. Second, an intra-module $i\text{SWAP}$ gate is performed between Q_2 and C_2 . This fully swaps the excitation from Q_2 to C_2 . Third, the photon is swapped between C_2 and C_4 across the router by pumping on the SQUID mode, just as demonstrated in Figure 2. The

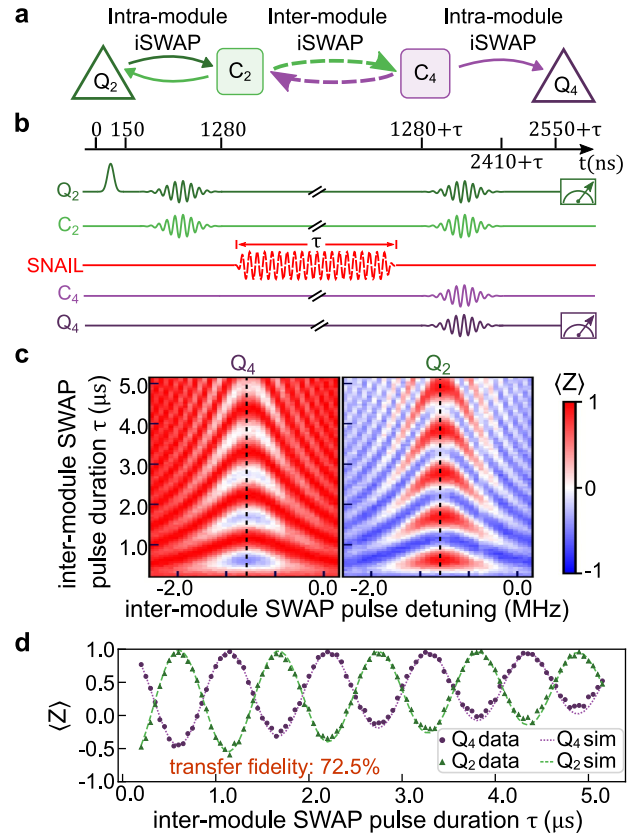


Figure 3. Fock state swap experiment between remote qubits. (a) Illustration of the photon swap protocol, in which a photon originating in Q_2 is fully swapped to C_2 , then depending on the variable inter-module pulse duration, routed to Q_4 or returned to Q_2 . (b) Experiment pulse sequence. A photon is created in Q_2 , then swapped to C_2 . Next, it is swapped (or not) to C_4 with a variable duration, inter-module $i\text{SWAP}$ pulse. Finally, the light in $C_{2,4}$ is routed via further intra-module $i\text{SWAPs}$ to their respective qubits, which are then measured. The upper black bar indicates the total experimental duration with τ describing the variable, SQUID actuated inter-module $i\text{SWAP}$. (c) Measurement result of Q_2 and Q_4 for different SQUID pump detuning and duration. Here, the color of the 2D sweep indicates the measurement along the qubits' z -axis. (d) A cut of the swap data along the dotted line indicated in (c). The green triangles and purple circles are Q_2 and Q_4 data, respectively, and the dashed lines are the corresponding simulation results.

SQUID pump duration is varied, which results in an effective Rabi oscillation between the two qubits when the protocol is completed. Finally, we apply two more intra-module $i\text{SWAP}$ gates, C_2 to Q_2 and C_4 to Q_4 . This fully transfers the states of C_2 and C_4 to their respective module qubits, which are then measured simultaneously using dispersive readout of the readout (R) modes. The results are shown in Fig. 3c and 3d. The transfer fidelity between Q_4 and Q_2 is $72.5 \pm 1.17\%$. We perform Lindblad master equation simulations assuming ideal interactions, with the only defects being all modes' measured

coherences (see Methods); the simulation results (dotted curves) show good quantitative agreement with our data, indicating that, as with coherent state operation, the primary fidelity limit in our system is the ratio of gate time to our modes' coherence times. The uncertainty given for the Fock state transfer fidelity, and all following quoted fidelities, is calculated following the 'bootstrap method' in^{53,54}. No correction is applied for State Preparation and Measurement (SPAM) errors. Details of our data processing and experimentally determined SPAM errors can be found in Methods and SI Sec. I.

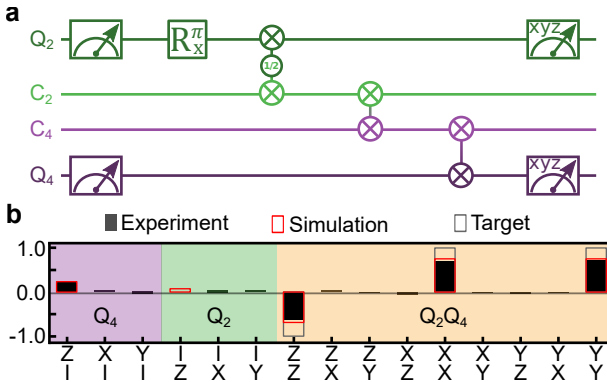


Figure 4. Inter-module Bell state generation. (a) Quantum circuit for generating a Bell state between Q_2 and Q_4 . Entanglement is first generated between Q_2 and C_2 using a $\sqrt{i\text{SWAP}}$ gate, then the cavity component is moved to Q_4 using two full- $i\text{SWAP}$ gates. (b) Tomography of the joint Q_2, Q_4 Bloch vector, in which each bar represents a joint measurement of the two qubits in the basis indicated (I indicates no measurement). Here, the black bars indicate the experimental result, the red rectangles are master-equation simulation results, and the gray rectangles represent the pure Bell state. The fidelity to the target Bell state $\frac{1}{\sqrt{2}}(|01\rangle + |10\rangle)$ is $76.9 \pm 0.76\%$, which agrees very well with the simulation prediction of 77.2%.

Inter-module Bell state generation. Next, we utilize a $\sqrt{i\text{SWAP}}$ gate, created by shortening the first intra-module $i\text{SWAP}$ gate from Figure 3 by close to 1/2 in duration, to create inter-module Bell states. The $\sqrt{i\text{SWAP}}$ has the effect of taking the single photon in the qubit and coherently 'sharing' it between the qubit and cavity, creating a Bell state between the two modes. Overall, the sequence first creates a Bell-pair inside a module, then shifts the communication cavity's component to a qubit in a second module. The quantum circuit is shown in Fig. 4a. Tomography is performed on both qubits, while the communication cavities are not measured. The measurement results are shown in Fig. 4b. From this tomographic data, we can reconstruct the density matrix of Q_2 and Q_4 , and find we achieve a Bell fidelity of $76.9 \pm 0.76\%$. The same experiment is performed on the other two qubit pairs $Q_2 - Q_3$ and $Q_4 - Q_3$ with fidelities of $58.7 \pm 2.40\%$ and $68.2 \pm 0.83\%$, respectively. The results were again compared with Lindblad master equa-

tion simulations (red rectangles in Fig. 4b), and show that the dominant source of infidelity remains the modes' lifetimes. In addition, we attempted a GHZ state preparation experiment between all three qubits in the modules using a similar scheme. The result is discussed in SI Sec. V.

Parallel operations. Another advantage of our architecture is that we can drive multiple parametric operations in the router simultaneously, which enables parallel operation and new ways to create entanglement. We demonstrate the simplest implementation of parallel operations by swapping light between two pairs of modules simultaneously. Here, M_2 and M_4 are treated as one sub-system, while M_3 and M_1 form a second. We swap a photon from Q_2 to Q_4 and Q_3 to C_1 across the router simultaneously. The gate sequence is shown in Fig. 5a. The two cross-module swap interactions, $C_2 - C_4$ and $C_3 - C_1$, are turned on simultaneously by pumping the SNAIL mode at the two difference frequencies using a room-temperature combiner. The SNAIL pumps are applied for a variable period. The protocol concludes with SWAP gates between all cavity-qubit pairs and measurement of all qubits.

The results (Fig. 5b) show that Fock states can swap between both pairs of modules simultaneously without interference or enhanced relaxation, as shown by comparison to master equation simulations. The drive frequencies for parallel swap processes in the router need frequency adjustments on the order of ~ 100 kHz compared to the single $i\text{SWAP}$ case, which we attribute to dynamic and static cross-Kerr effects due to the paired SNAIL drives. We reduce the pump strengths, slowing the gates from 600 ns to 1300 ns, as we observe additional decoherence when running two parallel processes at maximum pump strength. We do not believe this is a fundamental limitation, but can be improved in future experiment by optimized SNAIL and router design.

As further proof of the quantum coherence of parallel operations in the router, we repeat the Bell state generation protocol between Q_2 and Q_4 with the $M_1 - M_3$ $i\text{SWAP}$ activated in parallel. Again, the pump strengths are decreased, slowing the inter-module swap time. We achieve a Bell state fidelity of $68.1 \pm 0.79\%$, while the simulated fidelity is 68.4 %. Here, the decrease of fidelity compared to the single Bell state generation process (which has a fidelity of $76.9 \pm 0.76\%$) is due to the longer gate time used for the $C_2 - C_4$ $i\text{SWAP}$ in the presence of a parallel $i\text{SWAP}$ operation (see details in SI Sec. VII).

Multi-parametric gate experiment. To demonstrate further capabilities of our system, we also explored the use of two simultaneous swap processes that link one 'source' cavity to two 'target' cavities. We refer to such a processes as a 'V- $i\text{SWAP}$ '. This form of swap, for a certain duration, empties the source cavity, coherently and symmetrically swapping its contents into the target cavities. By combining the V- $i\text{SWAP}$ with a $(i\text{SWAP})^{2/3}$ gate (which is realized by turning on the $Q_2 - C_2$ ex-

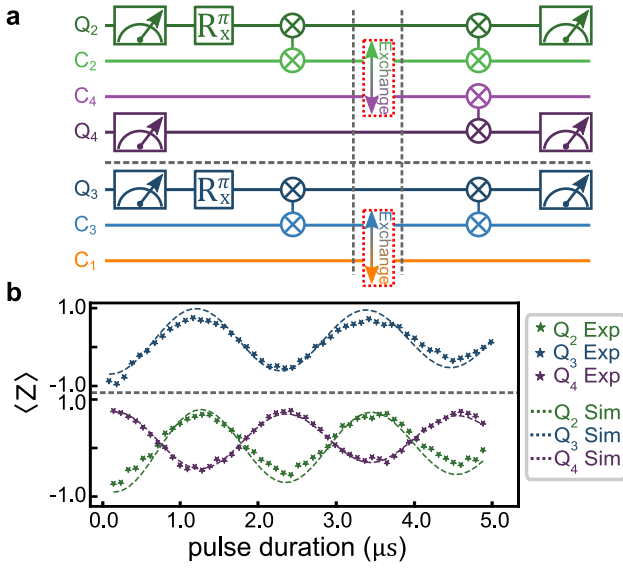


Figure 5. Parallel photon exchange experiment. (a) Gate sequence for parallel photon exchange over the router. (b) Photon population of all three qubits vs. router swap time. The dots are experimental results, and the corresponding dashed lines are simulation results.

change interaction for $t = \arctan(\sqrt{2})/g^{eff}$ as shown in Fig. 6a, we can take a single photon from Q_2 and create a W-state shared among the three designated modules. We achieve a fidelity of $53.4 \pm 2.56\%$ for this state. (see state reconstruction in Fig. 6b). For further discussion see SI Sec. III.C.

Currently, the utility of the above multi-parametric gates is limited by the slowdown of the gate times compared to individual *i*SWAPs. However, we believe this kind of multi-parametrically-pumped process should be further investigated, as it could be used to generate other multi-qubit gates in one step. Given the overhead in composing a multi-qubit gate from a series of two-qubit and single-qubit gates (for example, a Toffoli gate can be decomposed into 6 C-NOTs), performing these multi-parametric gates could give better performance in terms of gate fidelity by shortening the overall sequence time/gate count, even if operating at a lower rate.

We also note that in the above multi-parametric experiments, we observe no indication of fridge heating despite two strong pumps being applied to the SNAIL. Unlike on-resonance driving schemes that require large amounts of attenuation (usually 20-30 dB) on the mixing chamber (MC) plate to cool down higher-temperature noise, our off-resonance drive allows us to instead use a reflective low-pass filter on the SNAIL pump line (as shown in Extended Data Figure 1). This filter protects the modes in our device against high-temperature noise while allowing high-power, low-frequency signals to pass. So, the heat generated at the MC plate is actually very low even when the pump power is strong. Removal of the attenuators at the MC plate gives the parametric pumping scheme

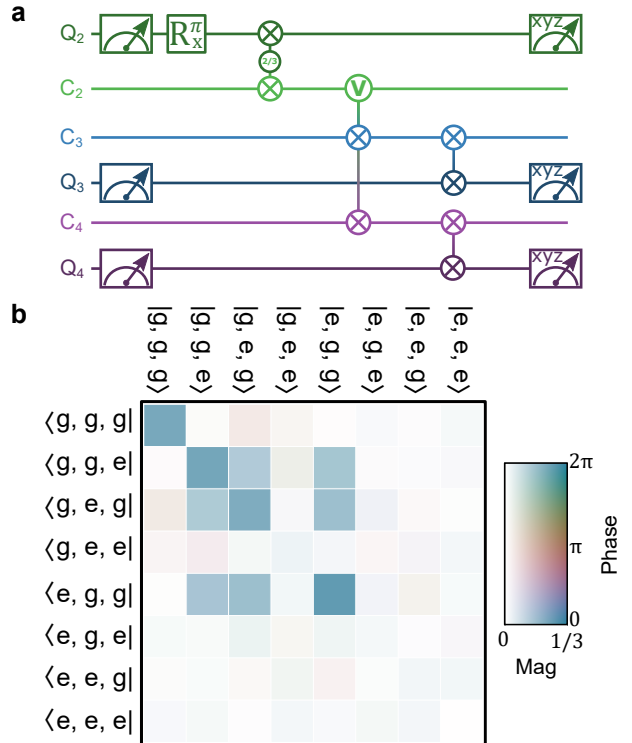


Figure 6. W state generation with ‘V-*i*SWAP’ gate. (a) W state generation pulse sequence. Together, the $(i\text{SWAP})^{2/3}$ and ‘V-*i*SWAP’ gates create a W state distributed across Q_2 , C_3 , and C_4 . The subsequent *i*SWAPs redirect the latter two components to Q_3 and Q_4 , respectively. (b) W state generation density matrix reconstructed from tomography. Each element in the density matrix is represented by a color using the Hue-Chroma-Luminance (HCL) color scheme. The amplitude of each element is mapped linearly to the Chroma and Luminance of the color, and the phase (from 0 to 2π) is mapped linearly to the Hue value. This color mapping scheme has the property that elements of the same amplitude are perceived equally by the human eye, so that the small magnitudes fade into the white background to avoid drawing the eye to small, noisy matrix elements. The observed fidelity of the state is $53.4 \pm 2.56\%$.

an advantage of 20-30 dB in fridge heating for the same circulating powers at base, which is an important step toward realizing large-scale/multiplexed qubit controls.

In the above discussion, we have listed only state fidelities, which are limited both by the mode lifetimes and the number of gates required to perform both intra- and inter-module operations in the same pulse sequence. Although our current device setup does not support tomography on the communication modules, we can estimate the performance of the router itself by considering the ‘average’ fidelity of the inter-module gates. Given the average gate time of $T_{gate,avg} \simeq 760$ ns, and the average decoherence time of our communication modes of $T_{C,avg} \simeq 22$ μ s we find $F_{avg} = 1 - \frac{T_{gate,avg}}{T_{C,avg}} = 0.97$.

IV. DISCUSSION AND OUTLOOK

We have demonstrated a coherent quantum state router for microwave photons and used it to realize a small, modular quantum computer. A key feature is the use of a SNAIL mode to create three-wave couplings in the router itself, rather than relying on nonlinear couplers embedded in each module. The router enables us to create all-to-all couplings among a set of quantum modules, to parametrically drive gates between the communication modes of those modules, and even to create three-qubit and perform parallel *i*SWAP operations between multiple pairs of communication modes by applying multiple, simultaneous parametric drives.

The current device's performance ($F_{avg} = 0.97$ for gates involving the router) is limited primarily by the qubit/cavity lifetimes involved, though the limitation is primarily in the modules themselves and due to imperfect quantum engineering. Other recent implementations of similar quantum modules^{25,50} have achieved much higher coherence time, with qubit and cavity modes in the $100 - 1000 \mu\text{s}$ range.

With modest improvements in the lifetime of our waveguide modes to $\sim 10 \mu\text{s}$, our router will be able to provide sub-microsecond, very high fidelity gates between millisecond-scale communication cavities. One way this can be achieved is by retracting the SNAIL and its related lossy elements (i.e. the bias magnet and the pump port) into a coupling tube^{55,56}. The tube works as a waveguide with a high cut-off frequency that limits the direct coupling between our waveguide modes and the lossy elements. The SNAIL can then maintain strong coupling to the waveguide modes with its antenna sticking into the waveguide. Such a design also has the advantage of coupling a single SNAIL to multiple router elements, allowing us to create inter-router operations and hence a scalable, modular network.

One vital question requires further research: How fast can we ultimately drive gates in this system? A straightforward route is to further increase the waveguide mode lifetimes in the router. We can then increase the dispersive coupling strength to their respective communication modes without decreasing the communication mode lifetimes. Doubling our current average coupling to $g/\Delta = 0.2$ will immediately push the average gate time to $\sim 100 \text{ ns}$. We must also explore further how hard the SNAILs can be driven with one or more drive tones. This is directly related to the issue of saturation power in parametric amplifiers, where recent exciting results^{39,57} provide guidance on how we may further optimize our router. With stronger module-router couplings, it is feasible to push our overall gate time down to $\sim 10 \text{ ns}$ in better optimized, next generation devices.

REFERENCES

- ¹Majumder, S., Andreta de Castro, L. & Brown, K. R. Real-time calibration with spectator qubits. *npj Quantum Information* **6**, 1–9 (2020).
- ²Krinner, S. *et al.* Benchmarking coherent errors in controlled-phase gates due to spectator qubits. *Physical Review Applied* **14**, 024042 (2020).
- ³Dai, X. *et al.* Calibration of flux crosstalk in large-scale flux-tunable superconducting quantum circuits. *PRX Quantum* **2**, 040313 (2021).
- ⁴Arute, F. *et al.* Quantum supremacy using a programmable superconducting processor. *Nature* **574**, 505–510 (2019).
- ⁵Cirac, J. I., Zoller, P., Kimble, H. J. & Mabuchi, H. Quantum State Transfer and Entanglement Distribution among Distant Nodes in a Quantum Network. *Phys. Rev. Lett.* **78**, 3221–3224 (1997). URL <https://link.aps.org/doi/10.1103/PhysRevLett.78.3221>. Publisher: American Physical Society.
- ⁶Kimble, H. J. The quantum internet. *Nature* **453**, 1023–1030 (2008). URL <https://www.nature.com/articles/nature07127>. Number: 7198 Publisher: Nature Publishing Group.
- ⁷Monroe, C. & Kim, J. Scaling the ion trap quantum processor. *Science* **339**, 1164–1169 (2013).
- ⁸Monroe, C. R., Schoelkopf, R. J. & Lukin, M. D. Quantum connections. *Scientific American* **314**, 50–57 (2016).
- ⁹LaRacuente, N., Smith, K. N., Imany, P., Silverman, K. L. & Chong, F. T. Short-range microwave networks to scale superconducting quantum computation. *arXiv preprint arXiv:2201.08825* (2022).
- ¹⁰McEwen, M. *et al.* Resolving catastrophic error bursts from cosmic rays in large arrays of superconducting qubits. *Nature Physics* **18**, 107–111 (2022).
- ¹¹Wilen, C. *et al.* Correlated charge noise and relaxation errors in superconducting qubits. *Nature* **594**, 369–373 (2021).
- ¹²Chou, C.-W. *et al.* Measurement-induced entanglement for excitation stored in remote atomic ensembles. *Nature* **438**, 828–832 (2005).
- ¹³Moehring, D. L. *et al.* Entanglement of single-atom quantum bits at a distance. *Nature* **449**, 68–71 (2007).
- ¹⁴Ritter, S. *et al.* An elementary quantum network of single atoms in optical cavities. *Nature* **484**, 195–200 (2012).
- ¹⁵Hofmann, J. *et al.* Heralded entanglement between widely separated atoms. *Science* **337**, 72–75 (2012).
- ¹⁶Bernien, H. *et al.* Heralded entanglement between solid-state qubits separated by three metres. *Nature* **497**, 86–90 (2013).
- ¹⁷Wengerowsky, S. *et al.* Entanglement distribution over a 96-km-long submarine optical fiber. *Proceedings of the National Academy of Sciences* **116**, 6684–6688 (2019).
- ¹⁸Yu, Y. *et al.* Entanglement of two quantum memories via fibres over dozens of kilometres. *Nature* **578**, 240–245 (2020).
- ¹⁹Roch, N. *et al.* Observation of measurement-induced entanglement and quantum trajectories of remote superconducting qubits. *Physical review letters* **112**, 170501 (2014).
- ²⁰Narla, A. *et al.* Robust concurrent remote entanglement between two superconducting qubits. *Physical Review X* **6**, 031036 (2016).
- ²¹Dicke, C. *et al.* Chip-to-chip entanglement of transmon qubits using engineered measurement fields. *Physical Review B* **97**, 064508 (2018).
- ²²Kurpiers, P. *et al.* Quantum communication with time-bin encoded microwave photons. *Physical Review Applied* **12**, 044067 (2019).
- ²³Monroe, C. *et al.* Large-scale modular quantum-computer architecture with atomic memory and photonic interconnects. *Phys. Rev. A* **89**, 022317 (2014). URL <https://link.aps.org/doi/10.1103/PhysRevA.89.022317>. Publisher: American Physical Society.
- ²⁴Linke, N. M. *et al.* Experimental comparison of two quantum computing architectures. *PNAS* **114**, 3305–3310 (2017). URL <https://www.pnas.org/content/114/13/3305>. Publisher: Na

tional Academy of Sciences Section: Physical Sciences.

²⁵Axline, C. J. *et al.* On-demand quantum state transfer and entanglement between remote microwave cavity memories. *Nature Physics* **14**, 705–710 (2018).

²⁶Campagne-Ibarcq, P. *et al.* Deterministic remote entanglement of superconducting circuits through microwave two-photon transitions. *Phys. Rev. Lett.* **120**, 200501 (2018). URL <https://link.aps.org/doi/10.1103/PhysRevLett.120.200501>.

²⁷Kurpiers, P. *et al.* Deterministic quantum state transfer and remote entanglement using microwave photons. *Nature* **558**, 264–267 (2018).

²⁸Leung, N. *et al.* Deterministic bidirectional communication and remote entanglement generation between superconducting qubits. *npj Quantum Inf* **5**, 1–5 (2019). URL <https://www.nature.com/articles/s41534-019-0128-0>.

²⁹Magnard, P. *et al.* Microwave quantum link between superconducting circuits housed in spatially separated cryogenic systems. *Physical Review Letters* **125**, 260502 (2020).

³⁰Sirois, A. J. *et al.* Coherent-state storage and retrieval between superconducting cavities using parametric frequency conversion. *Applied Physics Letters* **106**, 172603 (2015).

³¹McKay, D. C. *et al.* Universal gate for fixed-frequency qubits via a tunable bus. *Physical Review Applied* **6**, 064007 (2016).

³²Hazra, S. *et al.* Long-range connectivity in a superconducting quantum processor using a ring resonator. *arXiv preprint arXiv:2012.09463* (2020).

³³Noguchi, A. *et al.* Fast parametric two-qubit gates with suppressed residual interaction using the second-order nonlinearity of a cubic transmon. *Physical Review A* **102**, 062408 (2020).

³⁴Zhong, Y. *et al.* Deterministic multi-qubit entanglement in a quantum network. *Nature* **590**, 571–575 (2021). URL <https://www.nature.com/articles/s41586-021-03288-7>. Number: 7847 Publisher: Nature Publishing Group.

³⁵Frattini, N. *et al.* 3-wave mixing Josephson dipole element. *Applied Physics Letters* **110**, 222603 (2017).

³⁶Vlastakis, B. *et al.* Deterministically Encoding Quantum Information Using 100-Photon Schrödinger Cat States. *Science* **342**, 607–610 (2013). URL <https://science.sciencemag.org/content/342/6158/607>. Publisher: American Association for the Advancement of Science Section: Report.

³⁷Michael, M. H. *et al.* New Class of Quantum Error-Correcting Codes for a Bosonic Mode. *Phys. Rev. X* **6**, 031006 (2016). URL <https://link.aps.org/doi/10.1103/PhysRevX.6.031006>. Publisher: American Physical Society.

³⁸Gottesman, D., Kitaev, A. & Preskill, J. Encoding a qubit in an oscillator. *Phys. Rev. A* **64**, 012310 (2001). URL <https://link.aps.org/doi/10.1103/PhysRevA.64.012310>. Publisher: American Physical Society.

³⁹Sivak, V. *et al.* Kerr-Free Three-Wave Mixing in Superconducting Quantum Circuits. *Phys. Rev. Applied* **11**, 054060 (2019). URL <https://link.aps.org/doi/10.1103/PhysRevApplied.11.054060>. Publisher: American Physical Society.

⁴⁰Bergeal, N. *et al.* Analog information processing at the quantum limit with a Josephson ring modulator. *Nature Phys* **6**, 296–302 (2010). URL <https://www.nature.com/articles/nphys1516>.

⁴¹Sliwa, K. M. *et al.* Reconfigurable Josephson Circulator/Directional Amplifier. *Phys. Rev. X* **5**, 041020 (2015). URL <https://link.aps.org/doi/10.1103/PhysRevX.5.041020>. Publisher: American Physical Society.

⁴²Lecocq, F. *et al.* Nonreciprocal microwave signal processing with a field-programmable Josephson amplifier. *Physical Review Applied* **7**, 024028 (2017).

⁴³Nigg, S. E. *et al.* Black-Box Superconducting Circuit Quantization. *Phys. Rev. Lett.* **108**, 240502 (2012). URL <https://link.aps.org/doi/10.1103/PhysRevLett.108.240502>. Publisher: American Physical Society.

⁴⁴Minev, Z. K. *et al.* Energy-participation quantization of Josephson circuits. *npj Quantum Information* **7**, 1–11 (2021).

⁴⁵Bialczak, R. C. *et al.* Fast Tunable Coupler for Superconducting Qubits. *Phys. Rev. Lett.* **106**, 060501 (2011). URL <https://link.aps.org/doi/10.1103/PhysRevLett.106.060501>. Publisher: American Physical Society.

⁴⁶Motzoi, F., Gambetta, J. M., Rebentrost, P. & Wilhelm, F. K. Simple Pulses for Elimination of Leakage in Weakly Nonlinear Qubits. *Physical Review Letters* **103**, 110501 (2009). URL <https://link.aps.org/doi/10.1103/PhysRevLett.103.110501>.

⁴⁷Frattini, N., Sivak, V., Lingenfelter, A., Shankar, S. & Devoret, M. Optimizing the nonlinearity and dissipation of a SNAL parametric amplifier for dynamic range. *Physical Review Applied* **10**, 054020 (2018).

⁴⁸Planat, L. *et al.* Understanding the Saturation Power of Josephson Parametric Amplifiers Made from SQUID Arrays. *Phys. Rev. Applied* **11**, 034014 (2019). URL <https://link.aps.org/doi/10.1103/PhysRevApplied.11.034014>.

⁴⁹Liu, C., Chien, T.-C., Hatridge, M. & Pekker, D. Optimizing Josephson-ring-modulator-based Josephson parametric amplifiers via full Hamiltonian control. *Phys. Rev. A* **101**, 042323 (2020). URL <https://link.aps.org/doi/10.1103/PhysRevA.101.042323>.

⁵⁰Burkhart, L. D. *et al.* Error-detected state transfer and entanglement in a superconducting quantum network. *PRX Quantum* **2**, 030321 (2021).

⁵¹Sung, Y. *et al.* Realization of high-fidelity cz and z z-free iswap gates with a tunable coupler. *Physical Review X* **11**, 021058 (2021).

⁵²Pfaff, W. *et al.* Controlled release of multiphoton quantum states from a microwave cavity memory. *Nature Physics* **13**, 882–887 (2017).

⁵³Newman, M. E. & Barkema, G. T. *Monte Carlo methods in statistical physics* (Clarendon Press, 1999).

⁵⁴Young, P. *Everything you wanted to know about data analysis and fitting but were afraid to ask* (Springer, 2015).

⁵⁵Wang, C. *et al.* A schrödinger cat living in two boxes. *Science* **352**, 1087–1091 (2016).

⁵⁶Axline, C. J. *Building blocks for modular circuit QED quantum computing*. Ph.D. thesis, Yale University (2018).

⁵⁷Parker, D. J. *et al.* A near-ideal degenerate parametric amplifier. *arXiv preprint arXiv:2108.10471* (2021).

⁵⁸Place, A. P. *et al.* New material platform for superconducting transmon qubits with coherence times exceeding 0.3 milliseconds. *Nature communications* **12**, 1–6 (2021).

⁵⁹Breuer, H.-P., Petruccione, F. *et al.* *The theory of open quantum systems* (Oxford University Press on Demand, 2002).

⁶⁰Johansson, J. R., Nation, P. D. & Nori, F. QuTiP 2: A Python framework for the dynamics of open quantum systems. *Computer Physics Communications* **184**, 1234–1240 (2013). URL <https://www.sciencedirect.com/science/article/pii/S0010465512003955>.

METHODS

Device fabrication. The device in Fig. 1d contains a SNAL on a sapphire chip, three transmon qubits on individual sapphire chips, and multiple 3D resonator modes coupled with each other as shown in Fig. 1c. The coupling between the SNAL and waveguide modes is determined by the shape of the SNAL antenna (Extended Data Fig. 2b), which is fabricated using photolithography and acid etching from a 200-nm thin tantalum film on a c-plane sapphire substrate⁵⁸. Two windows were opened on the 3D waveguide above and below the SNAL chip in order to place a copper magnet and a pump port into the waveguide to enable flux bias and strong pumping (Extended Data Fig. 2a). The antennae of the transmon qubits are fabricated using the same tantalum etch-

ing technique, and both the SNAIL and transmon junctions are composed of Al-AlO_x-Al layers fabricated using a standard Dolan bridge method.

SNAIL mode characterization. The SNAIL mode is characterized by measuring the transmission signal from the SNAIL pump port to a side port on the waveguide using a network analyzer. By sweeping the bias current applied to the magnet (Extended Data Fig. 2c) we can measure how the frequency of the SNAIL and waveguide modes are changed by flux biasing the SNAIL loop.

Experimental setup. The modular quantum computer is installed at the base (~ 18 mK) plate of a cryogenic set-up (Extended Data Figure 1). Here, all pulse sequences are generated by a Keysight M3202A (1 GSa/s) and M3201A (500 MSa/s) Arbitrary Waveform Generators (AWGs). The baseband microwave control pulses are generated at an intermediate frequency

(IF) of 100 MHz and upconverted to microwave frequencies using IQ mixers. Image rejection (IR) mixers have been used for downconverting the detected signals to 50 MHz, which are then digitized using a control system based on Keysight M3102A Analog-to-Digital converters with a sampling rate of 500 MSa/s and on-board Field-Programmable Gate Arrays (FPGA) for signal processing.

Numerical simulations. We simulate the behavior of our system by analyzing the behavior of seven modes participating in the experiments: three qubit modes and four communication modes. We treat the gates as ideal parametric interactions, and work in the rotating frame of the system (details in SI sec III.A). The Hamiltonian then contains single-qubit controls, cavity-cavity inter-module interactions, and qubit-cavity intra-module interactions listed respectively to give:

$$\hat{\mathcal{H}}_{QC}/\hbar = \sum_{m=2,3,4} \eta_m (\hat{q}_m^\dagger + \hat{q}_m) + \sum_{\substack{i,j=1,2,3,4 \\ i \neq j}} \eta_{ij} g_{c_i c_j s} (\hat{c}_i^\dagger \hat{c}_j + \hat{c}_i \hat{c}_j^\dagger) + \sum_{k=2,3,4} \eta_k g_{q_k q_k c_k c_k} (\hat{c}_k^\dagger \hat{q}_k + \hat{c}_k \hat{q}_k^\dagger), \quad (5)$$

where \hat{q}_i indicates the qubit mode in each module and $\eta(t)$ represents the time-dependent strength of a given pulse, which follows the shapes and durations used in the experiment. To capture the effects of photon loss and decoherence in the system, we add loss operators with rates corresponding to the measured values listed in SI Table 1 and simulate the evolution of the system via the Lindblad master equation⁵⁹ using QuTiP⁶⁰:

$$\dot{\rho}(t) = -\frac{i}{\hbar} [\hat{H}_{QC}(t), \rho(t)] + \sum_n \mathcal{D} [\hat{C}_n] (\rho) \quad (6)$$

where ρ represents the density matrix of the system and $\mathcal{D}[\hat{C}_n](\rho) = \hat{C}_n \rho \hat{C}_n^\dagger - 1/2 (\hat{C}_n^\dagger \hat{C}_n \rho + \rho \hat{C}_n^\dagger \hat{C}_n)$ is the interaction between the system and the environment for different collapse operators.

For all experiments reported in the main text, we apply identical pulse sequences in the simulations, and record the final states after half of the measurement time (to account for decay during the measurement process). Results are consistent between experiments and simulation, which indicates that our device is primarily limited by the coherence times of our modes.

Data processing. For all quoted fidelities in the main text, we have first reconstructed the density matrix ρ from tomographic measurements, and for a given target state σ , the fidelity of the results is calculated using:

$$F(\rho, \sigma) = \left(\text{tr} \sqrt{\sqrt{\rho} \sigma \sqrt{\rho}} \right)^2. \quad (7)$$

Furthermore, a bootstrap method⁵⁴ has been used to estimate the uncertainty of the reported fidelity. In experiments, all final datasets contain more than 10,000 averages; we restructure the data set into $N_{\text{boot}} = 1,000$ data sets each containing $N = 10,000$ points obtained by Monte Carlo sampling of the original set of 10,000 points. During Monte Carlo sampling, the probability that a data point is picked is 1/N irrespective of whether it has been picked before. In the end, we calculate the standard deviation of the bootstrap data sets s_{x^B} .

In general, s_{x^B} should be related to the uncertainty of the original sample σ_x by:

$$\sigma_x = \sqrt{\frac{N}{N-1}} s_{x^B} \quad (8)$$

Since, in our case, $N = 10,000$ is sufficiently large, the square root can be replaced by unity.

DATA AVAILABILITY

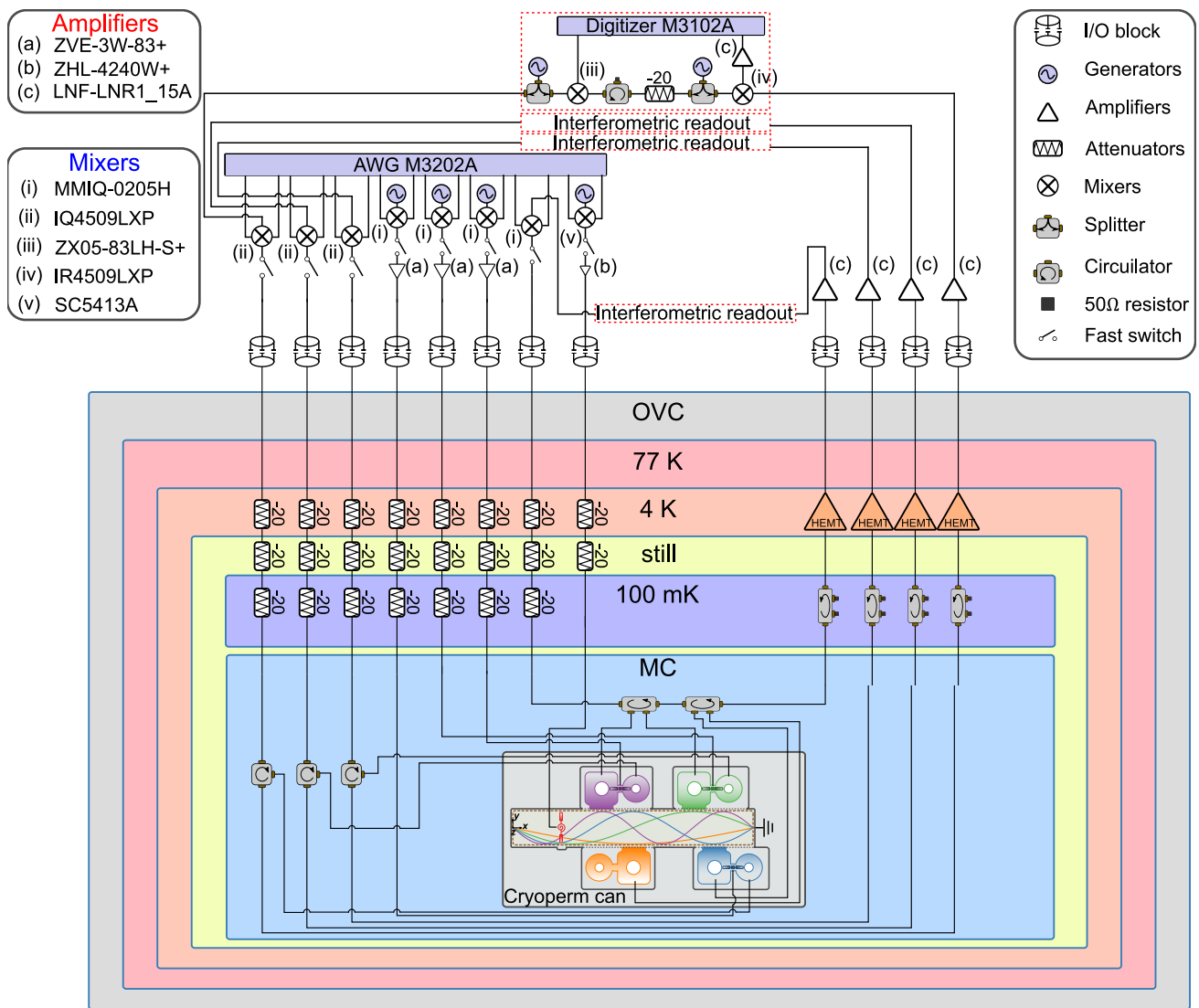
The data and code that support the findings of this study are available from the corresponding authors upon reasonable request.

ACKNOWLEDGEMENTS

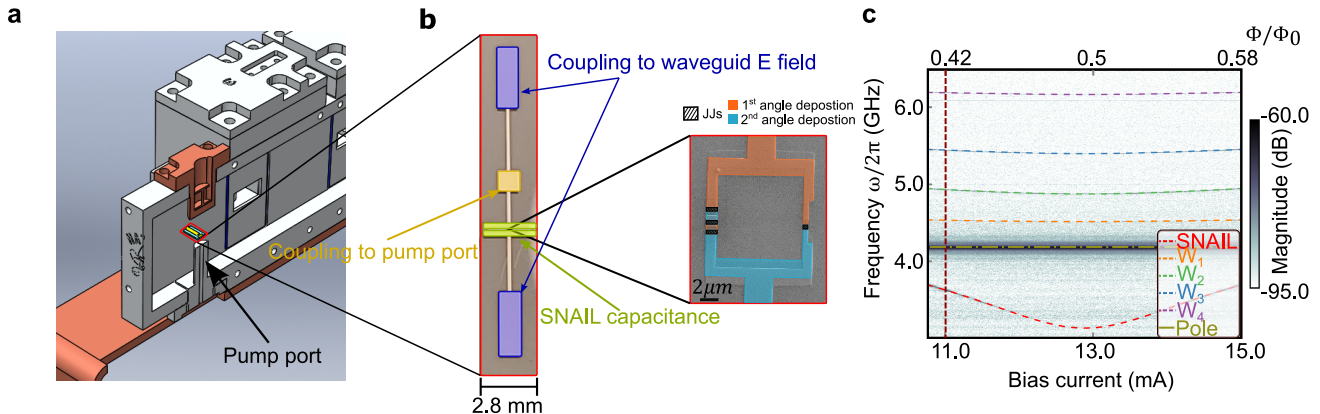
The authors gratefully acknowledge the skilled machining and advice of William Strang, and Shyam Shankar,

Kevin Chou, Konrad Lehnert, Alex Jones, Evan McKinney, and Robert Schoelkopf for fruitful discussions. We also acknowledge Keysight Technologies, especially Kevin Nguyen, for helping make the three-module portions of this experiment possible, and Alex Place and Andrew Houck for help in developing tantalum-based transmon and SQUID fabrication. This material is based

upon work supported by the Air Force Office of Scientific Research under award number FA9550-15-1-0015. This work was also partially supported by the Charles E. Kaufman Foundation of the Pittsburgh Foundation, as well as the Army Research Office under contracts W911NF-18-1-0144 and W911NF-15-1-0397.



Extended Data Figure 1. **Schematic of the experimental setup**



Extended Data Figure 2. **SNAIL mode details.** (a) Physical position of the SNAIL chip and pumping port. The SNAIL is flux-biased via a copper-sheathed electromagnet protruding into the waveguide above it, and is strongly coupled to a microwave drive line introduced via an aluminum cylinder below the SNAIL. (b) False color optical and SEM image of the SNAIL, indicating its essential components. (c) Color plot of the magnitude of transmission signal versus the frequency from SNAIL pumping port ($|S_{21}(\omega)|$) for a range of applied coil bias current/applied SNAIL flux. The dotted lines indicate the dressed modes of the waveguide modes and SNAIL, as well as the ‘pole mode’ of the aluminum cylinder containing the drive port. The vertical, dark-red dashed line indicates the operating flux of the SNAIL.

Supplementary Information for “A modular quantum computer based on a quantum state router”

Chao Zhou^{1†}, Pinlei Lu^{1†}, Matthieu Praquin², Tzu-Chiao Chien¹, Ryan Kaufman¹, Xi Cao¹, Mingkang Xia¹, Roger S. K. Mong¹, Wolfgang Pfaff³, David Pekker¹, Michael Hatridge¹

¹*Department of Physics and Astronomy, University of Pittsburgh, Pittsburgh, PA, USA*

²*Département de Physique, École Normale Supérieure, Paris, France*

³*Department of Physics, University of Illinois Urbana-Champaign, Champaign, IL, USA*

†*These authors contributed equally to this publication.*

(Dated: November 17, 2022)

CONTENTS

I. Mode parameters and frequency spectrum	2
II. Effect of exchange interaction VS mode type and state encoding	3
III. Parametric photon <i>i</i>SWAP gate using 3-wave-mixing	3
A. Parametric regime analysis	3
B. <i>i</i> SWAP gate time for all six cavity pairs	4
C. Multi-end router exchange	5
IV. Intra-module <i>i</i>SWAP	7
V. Inter-module GHZ state generation	8
VI. Exchange interaction leakage mitigation	8
VII. Generating Bell states during parallel operations	9
References	9

I. MODE PARAMETERS AND FREQUENCY SPECTRUM

Table S1 contains the measured parameters of all key modes in our device. All values have been directly measured and calibrated in the experiments at the operation bias point of the SNAIL. They are also used in our master equation simulations (see Methods, Numerical simulations in the main text). The measurement fidelity is calculated using single-qubit tomography. The single-qubit gate fidelity is measured using interleaved randomized benchmarking¹. In previous experiments we measured the router's waveguide mode frequencies and lifetimes, which we summarize in Table S2. The waveguide modes and SNAIL mode are primarily limited by coupling to the copper intrusion of the SNAIL's bias magnet and coupling to the SNAIL drive port. The latter's influence is reduced in the full experiment by the low-pass filter on its pump line. However, we did not directly measure waveguide mode lifetimes as the same filter renders them un-measurable via any port.

	Q_2	Q_3	Q_4	C_1	C_2	C_3	C_4	SNAIL
$\omega_0/2\pi$ (GHz)	3.067984	4.040709	3.566572	4.477662	4.812500	5.474195	6.180769	3.914900
T_1 (μ s)	60	9.1	8.4	23	27	13	20	0.98
T_{2R} (μ s)	18	6.3	8.0	45	47	11	23	1.0
T_{2E} (μ s)	24	7.6	8.0					
$\alpha/2\pi$ (MHz)	-141.3	-118.1	-125.8					
$\chi_{qc}/2\pi$ (MHz)	-0.11	-1.7	-0.86					
Measurement fidelity	93.6%	83.0%	88.0 %					
Single gate error	$0.48\% \pm 0.04\%$	$3.74\% \pm 0.5\%$	$3.21\% \pm 0.6\%$					

Table S1. Devices parameters.

	W_1	W_2	W_3	W_4
$\omega_0/2\pi$ (GHz)	4.534	4.936	5.446	6.190
T_1 (μ s)	1.68	0.29	0.28	0.81

Table S2. Waveguide mode lifetimes.

One natural advantage of our router design is that the parametric pumps are well-separated in frequency from all modes. This allows us to protect the quantum modes while still strongly pumping the parametric processes. As we can see from Fig S1, the communication modes and SNAIL mode itself are all at least 2 GHz higher than the parametric pumping frequencies.

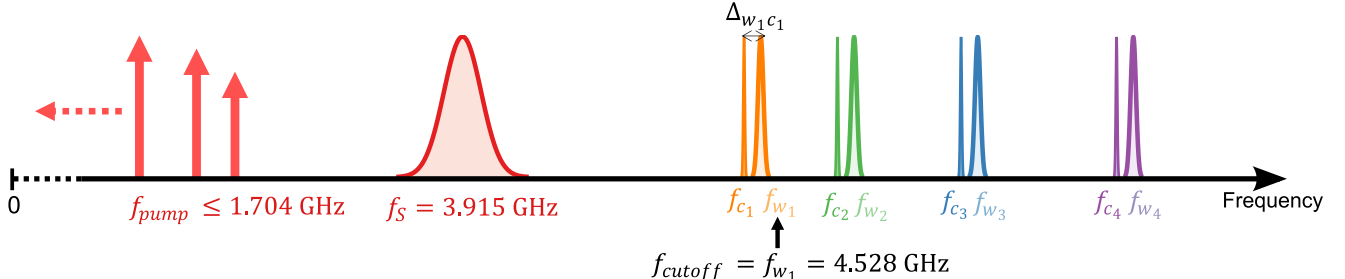


Figure S1. Frequency spectrum of all linear modes, SNAIL mode, and pumping frequencies. The maximum pumping frequency on the SNAIL is $f_{pump}^{max} \approx f_{c_4} - f_{c_1} = 1.704$ GHz, which is far below the waveguide cutoff frequency $f_{cutoff} = f_{w1} = 4.528$ GHz. The router then naturally protects pumping tones from propagating into modules. Meanwhile, the frequencies of all other modes don't have to be precisely controlled, so the router can be easily adapted to different modules without fine-tuning. Since the maximum pumping frequency is also lower than the SNAIL frequency $f_{pump}^{max} < f_s = 3.915$ GHz, a low-pass filter (e.g. Mini-Circuits VLF-2250+) is added to the SNAIL pump port so that strong pumps can be applied to SNAIL while the SNAIL mode lifetimes are protected.

II. EFFECT OF EXCHANGE INTERACTION VS MODE TYPE AND STATE ENCODING

As noted in the main text, depending on the qubit encoding in the Hilbert space of the state being swapped, the same parametric coupling (i.e. $\hat{\mathcal{H}}^{\text{eff}} = g_{c_i c_j}^{\text{eff}} (\hat{c}_i^\dagger \hat{c}_j + \hat{c}_i \hat{c}_j^\dagger)$) can result in very different state evolution. To clarify this, we compare different initial states and different kinds of modes (transmon qubit or cavity) at times $t = \pi/g^{\text{eff}}, 2\pi/g^{\text{eff}}, 3\pi/g^{\text{eff}}$ and $4\pi/g^{\text{eff}}$. In the following tables, the column labels indicate initial states, row labels indicate the unitary applied to the state, and the table values indicate the new state produced.

As shown in Table S3, the effective conversion process can perform a perfect *iSWAP* gate between two qubits. However, if the coupled objects include one linear mode, the situation becomes more complicated. For example, in the Fock state basis, the conversion process between two linear modes is more like a ‘beam splitter’ process^{2,3}; and in the coherent state basis, the process becomes a non-entangling exchange.

$ \psi_{\text{init}}\rangle$	$ 1, 0\rangle$	$ 1, 1\rangle$	$\alpha 0, 0\rangle + \beta 0, 1\rangle + \gamma 1, 0\rangle + \eta 1, 1\rangle$
$U^{1/2} \psi_{\text{init}}\rangle$	$\frac{1}{\sqrt{2}}(1, 0\rangle - i 0, 1\rangle)$	$ 1, 1\rangle$	$\alpha 0, 0\rangle + \frac{1}{\sqrt{2}}(\beta - i\gamma) 0, 1\rangle + \frac{1}{\sqrt{2}}(\gamma - i\beta) 1, 0\rangle + \eta 1, 1\rangle$
$U \psi_{\text{init}}\rangle$	$-i 0, 1\rangle$	$ 1, 1\rangle$	$\alpha 0, 0\rangle - i\gamma 0, 1\rangle - i\beta 1, 0\rangle + \eta 1, 1\rangle$
$U^{3/2} \psi_{\text{init}}\rangle$	$-\frac{1}{\sqrt{2}}(1, 0\rangle + i 0, 1\rangle)$	$ 1, 1\rangle$	$\alpha 0, 0\rangle - \frac{1}{\sqrt{2}}(\beta + i\gamma) 0, 1\rangle - \frac{1}{\sqrt{2}}(\gamma + i\beta) 1, 0\rangle + \eta 1, 1\rangle$
$U^2 \psi_{\text{init}}\rangle$	$- 1, 0\rangle$	$ 1, 1\rangle$	$\alpha 0, 0\rangle - \beta 0, 1\rangle - \gamma 1, 0\rangle + \eta 1, 1\rangle$

Table S3. Transmon to transmon exchange. We consider the final states of different initial states under evolution operation U^p , where U is defined as $U = \exp(-i\hat{\mathcal{H}}t)$, as $t = 2\pi/g^{\text{eff}}$. The exponent of U simply means $U^p = \exp(-i\hat{\mathcal{H}}(pt))$. Here, U^p creates an *iSWAP* family gate between the two qubits; $U^{1/2} = \sqrt{i\text{SWAP}}$ could be used to create a Bell state given an initial state $|1, 0\rangle$. Note that U performs an *iSWAP* gate, which is also a universal two-qubit gate that can create entanglement.

$ \psi_{\text{init}}\rangle$	$ 1, 0\rangle$	$ 1, 1\rangle$
$U^{1/2} \psi_{\text{init}}\rangle$	$\frac{1}{\sqrt{2}}(1, 0\rangle - i 0, 1\rangle)$	$\frac{1}{\sqrt{2}}(1, 1\rangle - i 0, 2\rangle)$
$U \psi_{\text{init}}\rangle$	$-i 0, 1\rangle$	$-i 0, 2\rangle$
$U^{3/2} \psi_{\text{init}}\rangle$	$-\frac{1}{\sqrt{2}}(1, 0\rangle + i 0, 1\rangle)$	$-\frac{1}{\sqrt{2}}(1, 1\rangle + i 0, 2\rangle)$
$U^2 \psi_{\text{init}}\rangle$	$- 1, 0\rangle$	$- 1, 1\rangle$

* Here, the unitary is defined as $U = \exp(-i\hat{\mathcal{H}}t')$, where $t' = t/\sqrt{2}$.

Table S4. Transmon to cavity exchange. We consider the Fock state basis as for transmon-cavity coupling, coherent states could result in an even more complicated scenario. Here, the U^p operator can still behave like a tunable beam-splitter if either the cavity or qubit is prepared to an empty/ground state. However, for initial states like $|1, n\rangle$, where $n \geq 1$, the U^p operator will no longer keep the state unchanged.

$ \psi_{\text{init}}\rangle$	$ 1, 0\rangle$	$ 1, 1\rangle$	$ \alpha, 0\rangle$	$ \alpha, \beta\rangle$
$U^{1/2} \psi_{\text{init}}\rangle$	$\frac{1}{\sqrt{2}}(1, 0\rangle - i 0, 1\rangle)$	$\frac{1}{\sqrt{2}}(2, 0\rangle + 0, 2\rangle)$	$ \alpha/2, -i\alpha/2\rangle$	$ \alpha/2 - i\beta/2, \beta/2 - i\alpha/2\rangle$
$U \psi_{\text{init}}\rangle$	$-i 0, 1\rangle$	$ 1, 1\rangle$	$ 0, -i\alpha\rangle$	$ -i\beta, -i\alpha\rangle$
$U^{3/2} \psi_{\text{init}}\rangle$	$-\frac{1}{\sqrt{2}}(1, 0\rangle + i 0, 1\rangle)$	$\frac{1}{\sqrt{2}}(2, 0\rangle + 0, 2\rangle)$	$ -i\alpha/2, -i\alpha/2\rangle$	$ -i\alpha/2 - i\beta/2, -\beta/2 - i\alpha/2\rangle$
$U^2 \psi_{\text{init}}\rangle$	$- 1, 0\rangle$	$ 1, 1\rangle$	$ -i\alpha, 0\rangle$	$ -i\alpha, -\beta\rangle$

Table S5. Cavity to cavity exchange. For two cavities prepared to Fock states, the U^p operator still behaves as a ‘beam splitter’. For the coherent state basis, it only exchanges coherent states between the two cavities, but will not create entanglement.

III. PARAMETRIC PHOTON *iSWAP* GATE USING 3-WAVE-MIXING

A. Parametric regime analysis

We now analyze the parametric exchange process in the system. Without loss of generality, we have excluded the qubit and readout cavity modes from the total Hamiltonian, and focused on the parametric coupling between the

communication cavities.

$$\hat{\mathcal{H}}_0/\hbar = \sum_{i=1,2,3,4} \left[\omega_{w_i} \hat{w}_i^\dagger \hat{w}_i + g_{w_i s} (\hat{w}_i^\dagger \hat{s} + \hat{w}_i \hat{s}^\dagger) \right] + \sum_{i=1,2,3,4} \left[\omega_{c_i} \hat{c}_i^\dagger \hat{c}_i + g_{c_i w_i} (\hat{c}_i^\dagger \hat{w}_i + \hat{c}_i \hat{w}_i^\dagger) \right] + \omega_s \hat{s}^\dagger \hat{s} + g_3 (\hat{s} + \hat{s}^\dagger)^3 \quad (1)$$

After re-diagonalizing the second-order terms in Eq. 1, all dressed modes in the router inherit third-order nonlinearity. The terms we use for the parametric pumping scheme are three-wave mixing terms:

$$g_{c_i c_j s} \left(\hat{c}_i^\dagger \hat{c}_j \hat{s} + \hat{c}_i \hat{c}_j^\dagger \hat{s}^\dagger \right), \quad (i, j = 1, 2, 3, 4; i \neq j). \quad (2)$$

Here, the \hat{c}_i and \hat{s} operators represent the dressed modes after re-diagonalization, and $g_{c_i c_j s}$ is the 3-wave-mixing coefficient. In the weak coupling regime where $(\frac{g}{\Delta})_{c_i w_i}, (\frac{g}{\Delta})_{w_i s} \sim 0.1$, the coefficient $g_{c_i c_j s} \approx g_3 (\frac{g}{\Delta})_{c_i w_i} (\frac{g}{\Delta})_{w_i s} (\frac{g}{\Delta})_{c_j w_j} (\frac{g}{\Delta})_{w_j s}$, where $\Delta_{w_i s} = \omega_{w_i} - \omega_s$.

To realize *iSWAP* gates between communication cavities based on Eq. 2, we apply a strong single-tone pump on the SNAIL at the frequency difference of two cavities, $\omega_p = |\omega_{c_i} - \omega_{c_j}|$, where $i, j = 1, 2, 3, 4; i \neq j$. The time-dependent pumping term can be written as $\hat{\mathcal{H}}_P/\hbar = \epsilon(t) (\hat{s} + \hat{s}^\dagger)$, where $\epsilon(t)$ is represented by:

$$\epsilon(t) = \begin{cases} \epsilon^x(t) \cos(\omega_p t) + \epsilon^y(t) \sin(\omega_p t), & 0 < t < t_g \\ 0, & \text{otherwise.} \end{cases} \quad (3)$$

Thus, the total system Hamiltonian under pumping can be written as $\hat{\mathcal{H}}' = \hat{\mathcal{H}}_0 + \hat{\mathcal{H}}_P$. To study the effect of this pumping term in the total Hamiltonian, we apply a unitary transformation on $\hat{\mathcal{H}}$ with displacement operator:

$$D(t) = \exp[(zs^\dagger - z^* s)], \quad (4)$$

where $z = -\frac{(\epsilon^x + i\epsilon^y)/2}{\omega_p - \omega_s} e^{-i\omega_p t} + \frac{(\epsilon^x - i\epsilon^y)/2}{\omega_p + \omega_s} e^{i\omega_p t}$. This results in a new Hamiltonian $\hat{\mathcal{H}}^D$, in which the $\hat{\mathcal{H}}_P$ term is canceled and $\hat{s} \rightarrow \hat{s} - z$. Specifically, the 3-wave mixing term in Eq. 2 becomes:

$$g_{c_i c_j s} \hat{c}_i^\dagger \hat{c}_j \left(\hat{s} \frac{(\epsilon^x + i\epsilon^y)/2}{\omega_p - \omega_s} e^{-i\omega_p t} - \frac{(\epsilon^x - i\epsilon^y)/2}{\omega_p + \omega_s} e^{i\omega_p t} \right) + h.c. \quad (5)$$

Then we apply a rotating frame transformation at the frequency of all the router modes (SNAIL + waveguide) and communication modes in the system:

$$R(t) = \exp \left[i\omega_s \hat{s}^\dagger \hat{s} + \sum_{i=1,2,3,4} i \left(\omega_{w_i} \hat{w}_i^\dagger \hat{w}_i + \omega_{c_i} \hat{c}_i^\dagger \hat{c}_i \right) \right], \quad (6)$$

Note that $\omega_p = |\omega_{c_i} - \omega_{c_j}|$. We assume that all the other frequency differences in the system are several linewidths away from the pumping frequency. Then the only slowly rotating term after the transformation is

$$\hat{\mathcal{H}}^{\text{RWA}}/\hbar = \eta g_{c_i c_j s} \left(\hat{c}_i^\dagger \hat{c}_j + \hat{c}_i \hat{c}_j^\dagger \right), \quad (7)$$

where $\eta = (\epsilon^x + i\epsilon^y) \omega_s / (\omega_d^2 - \omega_s^2)$. Here, η corresponds to the square root of the effective pump photon number in the SNAIL mode, i.e. $\eta \equiv \sqrt{n_s}$.

Equation 7 shows that pumping at $\omega_p = |\omega_{c_i} - \omega_{c_j}|$ activates the spontaneous photon exchange process between communication mode c_i and c_j . The *iSWAP* speed depends on the pumping strength and the three-wave mixing coefficient $g_{c_i c_j s}$. By controlling the length of the pulse, *iSWAP*^{1/n} gates can be performed between the two modes. Also, the existence of all the 3-wave-mixing terms between different modes allows us to pump multiple parametric processes simultaneously, e.g. we can perform *iSWAP* gate between two different cavity pairs at the same time by simultaneously pumping the SNAIL mode at the two difference frequencies.

B. *iSWAP* gate time for all six cavity pairs

By preparing coherent states in all four different cavities, we can perform six pairs of inter-module *iSWAPs*. We list all *iSWAP* gate times in Table S6. The average gate time is 760 ns.

<i>iSWAP</i> pair	<i>iSWAP</i> time (ns)
$C_1 \leftrightarrow C_2$	1248
$C_1 \leftrightarrow C_3$	651
$C_1 \leftrightarrow C_4$	535
$C_2 \leftrightarrow C_3$	942
$C_2 \leftrightarrow C_4$	832
$C_3 \leftrightarrow C_4$	375

Table S6. ***iSWAP* gate times between all six possible communication cavity pairs.** The data is measured by preparing a coherent state in one cavity and swapping it to another cavity. For each swap pair, the listed *iSWAP* gate time is based on the maximum *iSWAP* speed measured by tuning up the SNAIL pump power until we see obvious decrease of mode lifetime.

C. Multi-end router exchange

One benefit of the router design is that we can apply multiple pump tones on the SNAIL at the same time to activate multiple exchange processes simultaneously. This give us enhanced freedom for more complicated gates. In order to test this idea, we have designed two experiments: one realizing multiple exchanges in parallel, and a second realizing exchange from one source cavity to two target cavities (V-exchange).

The protocol and experimental results are shown in Fig. S2. All protocols are based on coherent states. First, we attempt the parallel exchange (as shown in SI. S2). Here, C_3 and C_4 have first been displaced with short Gaussian pulses, then the SNAIL pump is turned on such that $C_1 - C_4$ and $C_2 - C_3$ exchange is induced simultaneously. At the same time, the voltage output from all the cavities are measured through weakly-coupled ports. Comparing to the single exchange, a small, extra pump detuning (~ -250 kHz) is observed on both pumps, which we attribute to the dynamic-Kerr shift from the driven SNAIL⁴.

For the “V-exchange”, we have displaced C_2 first, then we turn on the SNAIL pumps for $C_2 - C_4$ and $C_2 - C_3$ exchange simultaneously, and similarly, we have recorded the voltage output from all three cavities. One thing is different from parallel exchange is that the rate of two exchanges between each pair need to be precisely identical. In our case, as C_3 and C_4 have been perfectly overlapped with each other, thus, C_2 to C_3 and C_2 to C_4 share the same exchange rate with each other. Again, a small extra pump detuning (~ -60 kHz) is added on both pumps to compensate for the dynamic-Kerr effect.

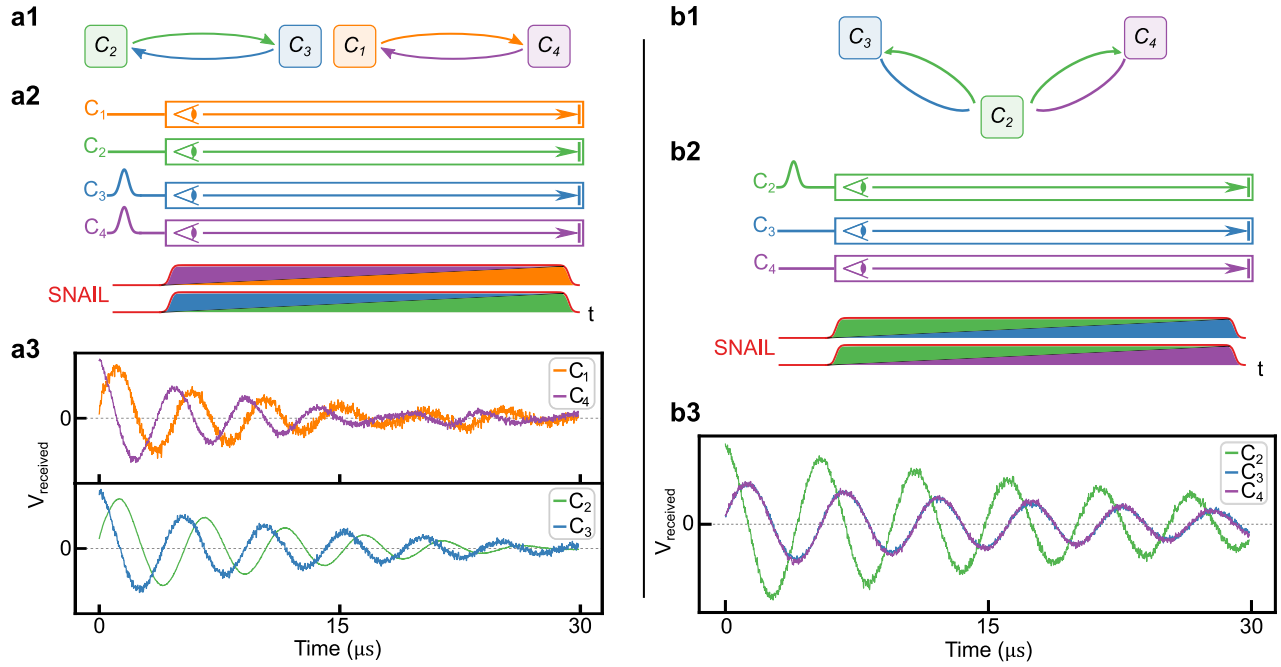


Figure S2. **Simultaneous exchanges between multiple cavities.** (a) Parallel exchange between C_1, C_4 and C_2, C_3 ; (a1, a2) Pulse sequence and schematic. (a3) We have rotated the output results so that the quadrature components equal to zero, and plot only the in-phase voltages vs time for all four cavities. (b) V-exchange from C_2 to C_3 and C_4 . In this case, the light can go back and forth between one cavity and two cavities. We have carefully tuned the pump frequencies and amplitudes so that the voltage trace for C_3 and C_4 perfectly overlap with each other. If C_2 is prepared to Fock state $|1\rangle$ at the beginning, and C_3 and C_4 are both prepared to empty states, then at the moment when C_2 is empty, a bell state would be created between C_3 and C_4 , as we have shown in main text Sec. III

IV. INTRA-MODULE *iSWAP*

The next ingredient, previously termed an intra-module *iSWAP*⁵, swaps information between qubits and communication cavities. In the experiment, the qubit is first prepared to its excited state, which gives module state $|e0\rangle$. Next, two side-band tones are applied near to the qubit and cavity frequencies. Here the detunings are around 10κ (~ 20 MHz) away from each mode to avoid any undesired mode excitation. Then, both *iSWAP* time and cavity side-band (CSB) detuning δ are swept to determine the optimized *iSWAP* condition. The average fidelity of a *iSWAP* gate is 94%, which is mainly limited by how fast the *iSWAP* gate is compared to T_1 and T_ϕ of qubit and cavity.

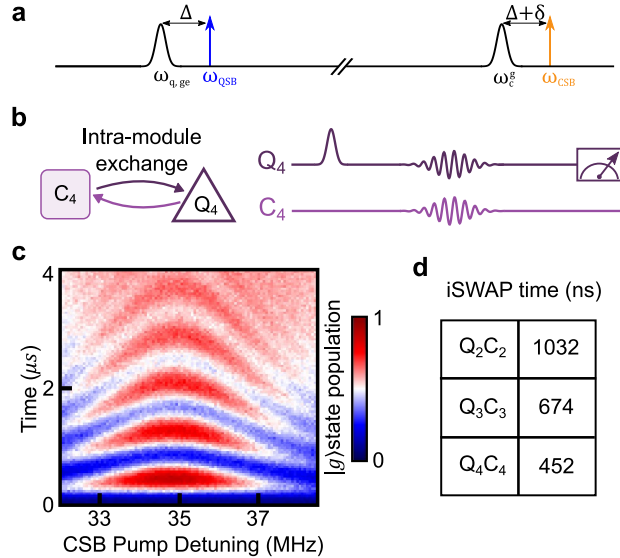


Figure S3. **Intra-module *iSWAP*.** (a) Schematic of qubit and communication cavity frequencies and pump tones. Two pump tones have been applied near the qubit and cavity frequencies to generate *iSWAP* between qubit and cavity. (b) Schematic and pulse sequence. The qubit is prepared in its excited state via a $R_x(\pi)$ pulse at $\omega_{q,ge}$, then two sideband pulses are applied at ω_{QSB} , detuned by Δ from $\omega_{q,ge}$, and ω_{CSB} , detuned by $\Delta + \delta$ from ω_c^g . Finally, projective measurement is applied to the qubit. Both pulse length, and δ are swept to determine an optimized *iSWAP* gate. (c) Rabi oscillation of the intra-module *iSWAP*. The vertical axis is the pulse time, and the horizontal axis is the CSB detuning δ , where the color indicates the $|g\rangle$ state population of qubit. (d) Full *iSWAP* time for all three cavity-qubit pairs in the system

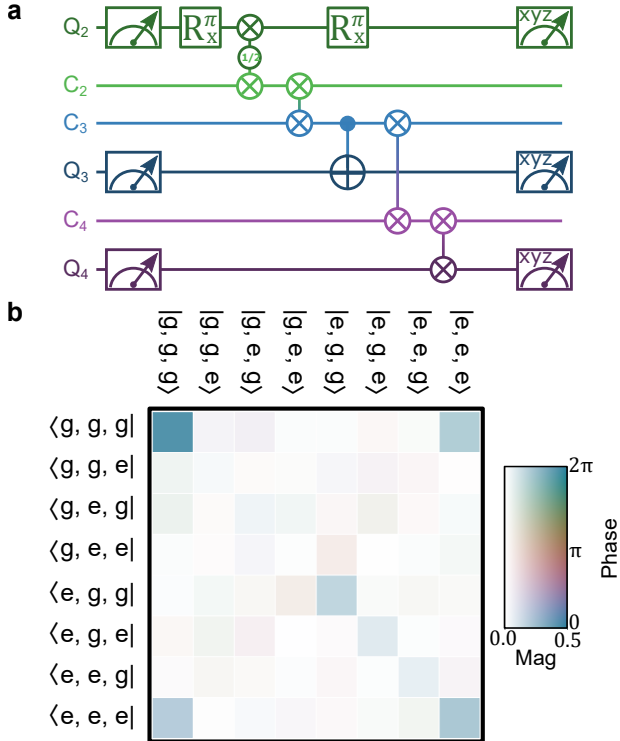


Figure S4. GHZ state generation experiment (a) GHZ state generation sequence. First, Q_2 is prepared to excited state, then an intramodule $\sqrt{i\text{SWAP}}$ gate is performed between Q_2 and C_2 , which creates a bell state between them. This entanglement is then transferred to C_3 via an inter-module $i\text{SWAP}$ gate. After that, an intra-module CNOT is performed between C_3 and Q_3 , which entangles Q_2 , Q_3 and C_3 . In the end, Q_2 state is flipped with a π pulse, and the photon in C_3 is transferred to Q_4 using two $i\text{SWAP}$ gate, which creates a GHZ state between Q_2 , Q_3 and Q_4 . (b) GHZ state generation density matrix reconstructed from tomography. Here, each element in the density matrix is represented with a color using the Hue-Chroma-Luminance (HCL) color scheme. The amplitude of each element is mapped linearly to the Chroma and Luminance of the color, and the phase (from 0 to 2π) is mapped linearly to the Hue value. This color mapping scheme has the property that elements of the same amplitude are perceived equally by the human eye, so that the small magnitudes fades into the white background to avoid drawing the eye to small, noisy matrix elements. The observed fidelity state is $48.9 \pm 5.27\%$

V. INTER-MODULE GHZ STATE GENERATION

Other than the W-state preparation demonstrated in the main text, we also performed a GHZ state preparation experiment between all three modules' qubits. The protocol in shown in Fig. S4a, this protocol requires one additional entangling gate: an intra-module CNOT. We achieve this using a state selective qubit π -pulse⁶. We reconstruct the final state from tomography as shown in Fig. S4b, and find a fidelity of $48.9 \pm 5.27\%$, just below the threshold for provable entanglement. While the result falls below the threshold for provable entanglement, it points to our ability to implement an extensive gate set in the router, and create multi-qubit entanglement.

VI. EXCHANGE INTERACTION LEAKAGE MITIGATION

Our router design contains intermediate waveguide modes which are close in frequency to the communication cavity modes. Thus, it is possible that when we pump an exchange process between two cavities strongly, their states could leak into to the neighbouring waveguide modes. Here we show how this leakage can be fixed using the idea of “derivative removal by adiabatic gate (DRAG)”⁷ at least for moderately long-lived waveguide modes.

Here we only consider the exchange process between two cavity modes c_1 and c_2 with their possible leakage to waveguide modes w_1 and w_2 . Following the same derivations as we have done in SI Sec.III.A, Eq. 1-5, to see the effect of the leakage to waveguide mode, we write the rotating frame transformation operator (Eq. 6) in a slightly different

way:

$$R'(t) = \exp \left[i\omega_s \hat{s}^\dagger \hat{s} + i(\omega_{c_1} - \delta/2) \hat{c}_1^\dagger \hat{c}_1 + i(\omega_{c_2} + \delta/2) \hat{c}_2^\dagger \hat{c}_2 + i(\omega_{c_1} - \delta/2) \hat{w}_1^\dagger \hat{w}_1 + i(\omega_{c_2} + \delta/2) \hat{w}_2^\dagger \hat{w}_2 \right], \quad (8)$$

where $\delta = \omega_{c_1} - \omega_{c_2} - \omega_p$. Then the Hamiltonian after RWA becomes:

$$\begin{aligned} \hat{\mathcal{H}}^{\text{RWA}}/\hbar = & \frac{\delta}{2} (\hat{c}_1^\dagger \hat{c}_1 - \hat{c}_2^\dagger \hat{c}_2) + (\delta/2 + \Delta_1) \hat{w}_1^\dagger \hat{w}_1 + (-\delta/2 + \Delta_2) \hat{w}_2^\dagger \hat{w}_2 \\ & + \eta (g_{c_1 c_2 s} \hat{c}_1^\dagger \hat{c}_2 + g_{c_1 w_2 s} \hat{c}_1^\dagger \hat{w}_2 + g_{c_2 w_1 s} \hat{c}_2^\dagger \hat{w}_1) + \text{h.c.}, \end{aligned} \quad (9)$$

where $\Delta_i = \omega_{w_i} - \omega_{c_i}$. Here, the cavity-cavity exchange term that we have seen in Eq. 7 still is present in Eq. 9. However, for $\eta g_{c_i w_j} \sim \delta + \Delta_j$ (strong pump), the effects of $\hat{c}_i^\dagger \hat{w}_j$ terms (waveguide-cavity exchange) can no longer be neglected. To study how this effect can be canceled using DRAG method, we introduce the adiabatic transformation V that allows us to work entirely in the cavity-cavity subspace. This transformation is

$$V(t) = \exp \left[-i\Re(\eta) \left(i \left(\frac{g_{c_1 w_2 s}}{\Delta_2 - \delta} \hat{c}_1 \hat{w}_2^\dagger + \frac{g_{c_2 w_1 s}}{\Delta_1 + \delta} \hat{c}_2 \hat{w}_1^\dagger \right) + \text{h.c.} \right) \right]. \quad (10)$$

After the adiabatic transformation, we have

$$\hat{c}_i \rightarrow \hat{c}_i + \Re(\eta) \zeta_i \hat{w}_j, \quad \hat{w}_j \rightarrow \hat{w}_j - \Re(\eta) \zeta_i \hat{c}_i \quad (11)$$

where $i, j = 1, 2; i \neq j$; $\zeta_1 = \frac{g_{c_1 w_2 s}}{\Delta_2 - \delta}$; $\zeta_2 = \frac{g_{c_2 w_1 s}}{\Delta_1 + \delta}$. After the transformation, the leakage terms: $\hat{c}_1^\dagger \hat{w}_2$ and $\hat{c}_2^\dagger \hat{w}_1$ become:

$$\frac{ig_{c_1 w_2 s} \omega_s}{\omega_d^2 - \omega_s^2} \left(\epsilon^y + \frac{\dot{\epsilon}^x}{\Delta_2 - \delta} \right) \hat{c}_1^\dagger \hat{w}_2 + \frac{ig_{c_2 w_1 s} \omega_s}{\omega_d^2 - \omega_s^2} \left(\epsilon^y + \frac{\dot{\epsilon}^x}{\Delta_1 + \delta} \right) \hat{c}_2^\dagger \hat{w}_1 + \text{h.c.}, \quad (12)$$

We find these terms can be cancelled under the condition:

$$\epsilon^y = -\frac{\dot{\epsilon}^x}{\Delta_2 - \delta} \text{ and } \epsilon^y = -\frac{\dot{\epsilon}^x}{\Delta_1 + \delta}. \quad (13)$$

Also, ac-Start shift (phase) error can be eliminated with the detuning δ that satisfies:

$$\delta/2 + \Re^2(\eta) \frac{g_{c_1 w_2 s}^2}{(\Delta_2 - \delta)^2} \left(-\Delta_2 + \frac{3}{2} \delta \right) = 0; \quad \delta/2 + \Re^2(\eta) \frac{g_{c_2 w_1 s}^2}{(\Delta_1 + \delta)^2} \left(\Delta_1 + \frac{3}{2} \delta \right) = 0 \quad (14)$$

Thus, we have eliminated the leakage to the nearest waveguide mode, however, we also notice that this frame induces the term $c_i^\dagger w_i$ with η^2 . This error can also be removed by adding higher transformation to the system, but because of the fact that we drive the system much detuned, this term can be ignored when $\eta \ll 1$.

VII. GENERATING BELL STATES DURING PARALLEL OPERATIONS

Due to the coherence time of all modes, the Bell states' fidelity has been limited by the *i*SWAP gate time in all operations. Here we use one example showing the limitation of the experiments. As we have mentioned in text, because of the saturation power when operating with multiple tones during parallel operations on the SNAI, we need to slow down the *i*SWAP rate. As shown in Fig. S5, when the *i*SWAP gate time increase from 600 ns to 1300 ns, the fidelity of bell states decrease from 76.9% to 68.1%. However, no additional side effect is added due to cross-talking or other source.

REFERENCES

¹J. Kelly, R. Barends, B. Campbell, Y. Chen, Z. Chen, B. Chiaro, A. Dunsworth, A. G. Fowler, I.-C. Hoi, E. Jeffrey, *et al.*, “Optimal quantum control using randomized benchmarking,” *Physical review letters* **112**, 240504 (2014).
²W. Pfaff, C. J. Axline, L. D. Burkhardt, U. Vool, P. Reinhold, L. Frunzio, L. Jiang, M. H. Devoret, and R. J. Schoelkopf, “Controlled release of multiphoton quantum states from a microwave cavity memory,” *Nature Physics* **13**, 882–887 (2017).

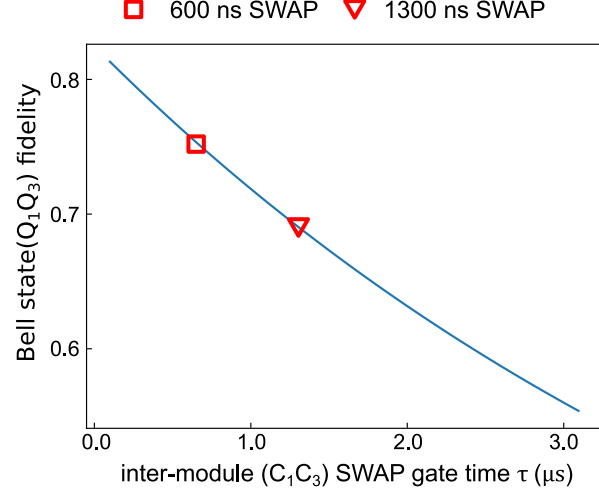


Figure S5. Bell stated fidelity versus inter-mdoule *i*SWAP gate time. The blue line represents the simulation of the bell state fidelity between Q_1 and Q_3 when we varying the inter-module *i*SWAP gate time. The 600 ns (1300 ns) *i*SWAP corresponding to the Bell state generation without (with) parallel operations.

³L. D. Burkhardt, J. D. Teoh, Y. Zhang, C. J. Axline, L. Frunzio, M. Devoret, L. Jiang, S. Girvin, and R. Schoelkopf, “Error-detected state transfer and entanglement in a superconducting quantum network,” PRX Quantum **2**, 030321 (2021).

⁴V. Sivak, N. Frattini, V. Joshi, A. Lingenfelter, S. Shankar, and M. Devoret, “Kerr-Free Three-Wave Mixing in Superconducting Quantum Circuits,” Phys. Rev. Applied **11**, 054060 (2019), publisher: American Physical Society.

⁵A. Narla, S. Shankar, M. Hatridge, Z. Leghtas, K. M. Sliwa, E. Zalys-Geller, S. O. Mundhada, W. Pfaff, L. Frunzio, R. J. Schoelkopf, *et al.*, “Robust concurrent remote entanglement between two superconducting qubits,” Physical Review X **6**, 031036 (2016).

⁶D. Schuster, A. A. Houck, J. Schreier, A. Wallraff, J. Gambetta, A. Blais, L. Frunzio, J. Majer, B. Johnson, M. Devoret, *et al.*, “Resolving photon number states in a superconducting circuit,” Nature **445**, 515–518 (2007).

⁷F. Motzoi, J. M. Gambetta, P. Rebentrost, and F. K. Wilhelm, “Simple Pulses for Elimination of Leakage in Weakly Nonlinear Qubits,” Physical Review Letters **103**, 110501 (2009).